








**Unusual dynamics of the ferroelectric phase transition in  $K_{1-x}Li_xTaO_3$  crystals**

D. Nuzhnyy <sup>\*</sup>, V. Bovtun , E. Buixaderas , J. Petzelt , M. Savinov, M. Kempa , M. Paściak,  
I. Rafalovskyi, V. Chelod Paingad, P. Kužel, and S. Kamba   
*Institute of Physics of the Czech Academy of Sciences, Prague, Czech Republic*

D. Repčák 


*Institute of Physics of the Czech Academy of Sciences, Prague, Czech Republic  
and Faculty of Nuclear Sciences and Physical Engineering, Czech Technical University in Prague, Czech Republic*

A. Pashkin 

*Institute of Ion Beam Physics and Materials Research, Helmholtz-Zentrum Dresden-Rossendorf, Dresden, Germany*

V. A. Trepakov

*Ioffe Physical-Technical Institute RAS, St. Petersburg, Russia*

Z. Trybuła 

*Institute of Molecular Physics, Polish Academy of Sciences, Poznań, Poland*



(Received 10 February 2022; revised 12 April 2022; accepted 25 April 2022; published 9 May 2022)

$K_{1-x}Li_xTaO_3$  ( $x = 0.043, 0.08$ ) crystals, characterized by pyroelectric current with calculated spontaneous polarization and zero-field second-harmonic generation, have been studied by broadband dielectric spectroscopy, including time-domain terahertz transmission and infrared (IR) reflectivity, and by polarized Raman spectroscopy in the 10–300 K temperature range. This multiexperimental approach has proven the percolative nature of the ferroelectric (FE) transition at low temperatures and demonstrated that the FE phase is inherently inhomogeneous and displays coexistence of FE and relaxor regions. Thanks to the very broad frequency range studied (from 1 Hz to 20 THz), the relevant excitations were identified and fitted in the dielectric response of both crystals: three relaxations, a central mode (CM), and a soft mode (SM) that splits into three components on cooling. Two Cole-Cole relaxations (assigned to flipping of polar nanoregions around the  $Li^+$  ions by  $\pi/2$  and  $\pi$ , in agreement with the known literature), thermally activated below  $\sim 150$  K, but staying in the gigahertz range at higher temperatures, do not show any frequency anomaly at the FE transition and are therefore related to the non-FE parts of the sample volume. A third thermally activated relaxation of unusually slow dynamics was revealed at low frequencies and preliminary assigned to an expected critical relaxation connected with the percolative nature of the FE phase transition. The IR SM, which undergoes much less softening than in the undoped  $KTaO_3$ , splits into three components below the FE transition. Two higher-frequency components correspond to the FE volume part of the crystals assigned to the split  $A_1$  and  $E$  modes due to the cubic-tetragonal transition. The third low-frequency component is assigned to the non-FE (relaxor) volume part. Our assignment was confirmed by modeling the terahertz-IR response of the SM using the Bruggeman model within the effective medium approach. Below the SM response, an additional CM in the  $10^{11}$  Hz range in the whole temperature range is inferred from the fits.

DOI: [10.1103/PhysRevB.105.184103](https://doi.org/10.1103/PhysRevB.105.184103)

**I. INTRODUCTION**

Li-doped  $KTaO_3$  ( $K_{1-x}Li_xTaO_3$ , KLT100 $x$ ) is one of the best-known doped incipient ferroelectric (FE) systems with relaxor-FE properties studied since the 1970s [1]. It forms a mixed crystal system with isovalent mixing on the A site of the  $ABO_3$  perovskite structure, unlike the usual Pb-containing relaxors with aliovalent mixing on the B site. It is known to display a dipolar glass or relaxor behavior at low  $Li^+$

concentrations (low  $x$ ) but undergoes a FE phase transition for  $x > 0.022$  with a first-order transition temperature  $T_C \geq 40$  K [2], increasing with  $x$ , see also the reviews [3–5]. Pure  $KTaO_3$  (KTO) is a well-known incipient FE and quantum paraelectric without any phase transition. Its permittivity increases on cooling up to  $\sim 4000$ , but below  $\sim 10$  K, it levels off [5,6]. The permittivity increase is entirely due to softening of the terahertz soft mode (SM) as in ideal displacive FEs. Due to the much smaller size, the  $Li^+$ -ion dopants are strongly off-center (by  $\sim 1$  Å in the [001] directions of the perovskite unit cell [7]), and their dynamic hopping among the six (001) off-center sites in the unit cell produces a rather complex

<sup>\*</sup>nuzhnyj@fzu.cz

dielectric dispersion below the SM frequency range [3,4], and due to the coupling to SM, the SM softening is strongly reduced [8,9]. The main relaxational dispersion in the standard low-frequency range of the dielectric spectroscopy (LF, up to  $\sim 1$  MHz) occurs only at relatively low temperatures ( $< 70$  K); at higher temperatures, it shifts up to the less-studied high-frequency range (HF, MHz-GHz). At low  $x$ , one thermally activated relaxation dominates the LF spectra, but two relaxation regions were observed in the spectra above the critical concentration  $x_c \approx 0.022$  [10–13]. The stronger and higher-frequency relaxation with lower activation energy ( $\sim 1000$  K) in the Arrhenius law is assigned to individual  $\text{Li}^+$  ion hopping among the six off-center sites corresponding to the unit-cell dipole-moment reorientations among the [001] directions by  $\pi/2$  and small polar nanoclusters (PNCs) of the polarized KTO matrix around them. Based on first-principles calculations [14], the slower relaxation was assigned to correlated reorientations by  $\pi$  of the nearest-neighbor Li-ion pairs, both off-centered in the same direction (with the distorted adjacent KTO unit cells attached to them). Its activation energy is higher (2100–2800 K), and the relaxation is spectrally broader, corresponding to a broader distribution of the relaxation times, attributed to various PNC sizes and random fields.

The understanding of the development of polar correlations on approaching  $T_C$  can be derived from various structural experiments, including neutron [15] and x-ray scattering [16] as well as the first-principles calculations [7,14]. The latter have shown that the [100] displacement of Li ions causes the relaxation of positions of the nearby ions and creation of strongly anisotropic, small needle-shaped PNCs that possess a dipole moment  $\sim 5$  times larger than that of the off-centered Li itself [14]. The PNCs centered on single Li ions or Li-Li nearest-neighbor pairs interact and correlate over larger distances creating polar nanoregions (PNRs). The correlation lengths within the PNRs have been estimated by various experiments to be in the range from several nanometers (neutron diffuse scattering above  $T_C$  [15]) to tens of nanometers (second harmonic generation (SHG) [17]). In a single PNR, the dipole moments of PNCs fluctuate in phase even if they do not touch each other necessarily. The local structure in the FE phase below  $T_C$  is not so well understood, but the freezing below  $T_C$  connected with a first-order FE transition can be understood as a percolation threshold of the PNRs due to their increasing size and merging into microdomains [18]. This threshold is associated with the tetragonal distortion that can host domains of two opposite orientations (quadrupolar order) and hence encompass larger-scale areas [17,19]. The percolation scenario also implies that not the whole volume undergoes the FE transition; part of the volume contains localized PNRs, as in the relaxor phase above  $T_C$ . Nevertheless, the consequences of this effect have not been investigated yet.

In this paper, we would like to pay attention to the broad-frequency dielectric responses of KLT crystals with higher  $x$  which undergo FE phase transitions, including their behavior around and below  $T_C$ . Several samples of this type were already studied [1,3–5,10,12,13], but the dielectric behavior near and across  $T_C$  was not discussed. In the past, our group studied the infrared (IR) reflectivity, time-domain terahertz transmission, and broadband dielectric response up to the microwave (MW) range [20,21] of KLT crystals with

$x \approx 0.06$  without observing any anomaly at  $T_C \approx 70$  K ( $T_C$  determined from the SHG on zero-field cooling [22]). The main result was the reduced SM softening compared with that in undoped KTO and less doped KLT, in agreement with the hyper-Raman spectroscopy [9]. Here, we report our studies on KLT4.3 and KLT8 single crystals, which on zero-field cooling, undergo first-order FE transitions at  $T_C \approx 50$  K [23] and  $T_C \approx 109$  K [24,25], respectively. We present measurements of the spontaneous polarization  $P_s$ , SHG, and broadband dielectric spectroscopy in the 5–300 K range including LF (1– $10^6$  Hz), HF ( $10^6$ – $10^9$  Hz), MW data  $\sim 5.8$  GHz, terahertz (0.2–2 THz), IR reflectivity (2–20 THz), and polarized Raman spectroscopy. The LF dielectric properties of these samples were independently studied in Refs. [23,24]. Raman and hyper-Raman spectroscopy on similar samples were discussed and compared in detail by Vogt [8,9,26–28]. The dielectric and Raman data were more recently published also on ceramics of similar Li compositions ( $x = 0.05$  and  $0.1$ ) [29,30] and will be compared with ours. Our data strongly suggest that the FE phases in KLT4.3 and KLT8 are inherently inhomogeneous since they feature a coexistence of the FE and relaxor nanoregions.

## II. EXPERIMENTAL DETAILS

The KLT single crystals were grown by a slow cooling method from the flux [31] and were LF dielectrically characterized in Refs. [23,24]. They were prepared as thin plane-parallel polished plates with thicknesses of  $\sim 0.55$  mm. The SHG measurements were performed without external electric field using a setup powered by a Ti:sapphire femtosecond laser amplifier (Spitfire ACE) with output at 800 nm, 40 fs pulse length, and 5 kHz repetition rate. Samples placed in a continuous-flow cryostat were illuminated by a collimated beam with a fluence of  $2.5$  mJ/cm<sup>2</sup>. After appropriate spectral filtering, the SHG signal generated in transmission configuration was detected by an avalanche photodiode.

For the dielectric measurements, Au-Pd electrodes were deposited using a Bal-Tec SCD 050 sputter coater on the principal faces of the plates. Silver wires fixed to the electrodes by a silver paint were used as electric contacts. LF dielectric permittivity and losses (1 Hz–1 MHz) were measured in the 5–300 K range on cooling using a Novocontrol Alpha-AN High-Performance Frequency Analyzer in conjunction with a Janis ST-100 cryostat with temperature controller Lakeshore 335. The temperature rate and the applied AC electric field was  $\sim 1.5$  K/min and 20 V/cm, respectively. The pyrocurrent measurements under zero-field heating with the 5 K/min rate after cooling in the  $E$  field of 3 kV/cm were performed using the Electrometer High Resistance Meter KEITHLEY 6517B. All other measurements were carried out without external  $E$  field.

For the dielectric measurements in the HF (1 MHz–1 GHz) and MW ( $\sim 5.8$  GHz) range the coaxial-line impedance measurement and a dielectric resonator technique were applied, respectively. Complex input impedance of the shorted coaxial line with cylindrical sample ( $\sim 2$  mm long and  $\sim 2$  mm in diameter), inserted in the gap between the inner conductor and short, was measured in the HF range between 100 and 350 K. A computer-controlled dielectric spectrometer

consisting of the Agilent 4291B RF impedance analyzer, Novocontrol BDS 2100 coaxial sample cell, and Sigma Systems M18 temperature chamber with liquid nitrogen cooling, was used for recording the HF impedance spectra on cooling with a temperature rate of 1 K/min. The complex dielectric permittivity was calculated accounting for the electromagnetic field distribution in the sample. For the MW measurements, we used the composite dielectric resonator method [32–34].  $TE_{01\delta}$  resonance frequency, quality factor, and insertion loss of the base cylindrical dielectric resonator with and without the sample were recorded during heating from 10 to 400 K with a temperature rate of 0.5 K/min in a Janis closed-cycle He cryostat. Thin disk-shaped samples without electrodes (thicknesses 50 and 70  $\mu\text{m}$  for KLT4.3 and KLT8, respectively) were placed on top of the base resonator. The resonators were measured in the cylindrical shielding cavity using the transmission setup with a weak coupling by an Agilent E8364B network analyzer. Dielectric parameters of the samples were calculated from the measured resonance frequencies (single frequency  $\sim 5.8$  GHz at each temperature) and quality factors of the base and composite resonators.

IR reflectivity spectra were measured at near-normal incidence using the Fourier transform IR spectrometer Bruker IFS 113v equipped with Si bolometer detector operating at 1.6 K in the range of 1–20 THz. Complex terahertz dielectric spectra in the range of  $\sim 0.2$ –2 THz in the transmission mode were obtained from thin plane-parallel samples (the same as for the MW measurements) using a custom-made time-domain terahertz transmission spectrometer powered by a femtosecond laser oscillator [35]. Continuous-flow He cryostats (Optistat, Oxford) with mylar and polyethylene windows were used for the terahertz and IR experiment, respectively.

Raman scattering was excited with the 514.5 nm line of an Ar laser at a power of 25 mW, and the spectra were recorded in backscattering geometry using the RM-1000 Renishaw Raman microscope. A Bragg filter enabled good stray light rejection and provided the scattered signal in the 5–900  $\text{cm}^{-1}$  ( $\sim 0.2$ –30 THz) range. The temperature-dependent spectra (10–300 K) were acquired using a continuous-flow He cryostat (Oxford Instruments), and the microscope was equipped with a special angled arm carrying a 20 $\times$  ultralow watt density objective for efficient optical coupling. The diameter of the laser spot on the sample surface was  $\sim 5$   $\mu\text{m}$ , and the spectral resolution was  $< 2$   $\text{cm}^{-1}$ . The spectra were recorded using the polarized light and corrected for the instrumental function of the microscope and the Bose-Einstein thermal factor.

### III. RESULTS

#### A. Spontaneous polarization and SHG

Temperature dependences of the spontaneous polarization  $P_s$  obtained from the pyroelectric current of KLT4.3 and KLT8 are shown in Fig. 1. Our data are compared with the data in Refs. [23,24]. One can see similar phase transition temperatures but different values of  $P_s$  caused presumably by lower poling fields and different samples used in Refs. [23,24]. Let us note that the standard procedure of obtaining  $P_s$  in FEs from the hysteresis loops is known to be inefficient in KLT

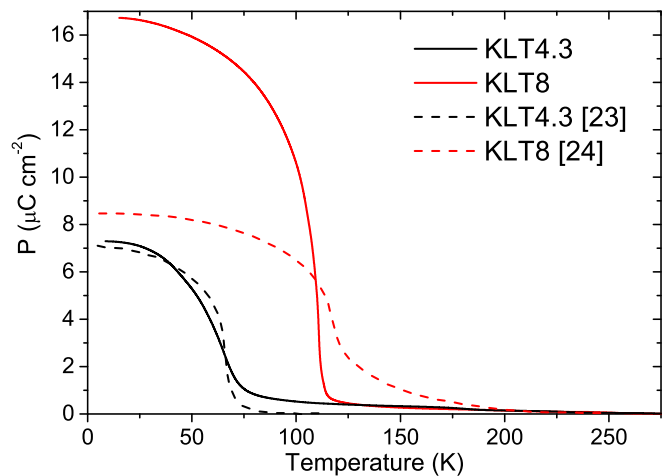


FIG. 1. Temperature dependence of  $P_s$  in KLT4.3 and KLT8 calculated from the pyrocurrent measurements on zero  $E$ -field heating (5 K/min) after cooling down with  $E = 3$   $\text{kV cm}^{-1}$  (solid lines). Similar data using  $E = 0.83$   $\text{kV cm}^{-1}$  for KLT4.3 [23] and  $E = 1.78$   $\text{kV cm}^{-1}$  for KLT8 [24] (dashed lines) are shown for comparison.

[3,23–25,29] due to insufficient maximal possible applied field, which we confirmed by our own attempts.

The SHG signal is permitted by symmetry only in off-center symmetry crystals. Therefore, we can expect appearance of the SHG signal in the FE phase below  $T_C$  and weakly also above  $T_C$  in the temperature range where the PNRs appear. Results of our experiments on cooling down to 20 K and subsequent heating are shown in Fig. 2. Thermal hysteresis of  $\sim 10$  K between the cooling and heating is seen in both samples, not being caused by the thermal contact since the samples were placed in a He gas bath, and the temperature rate was 0.6 K/min only. It is comparable with that determined from the temperature dependence of the LF permittivity [23,25]. It indicates the first-order nature of the phase transition in both samples, known also from the previous SHG experiments [16,17,36–38], and our values of  $T_C$  on heating agree with the  $P_s(T)$  dependences in Fig. 1. The SHG signal

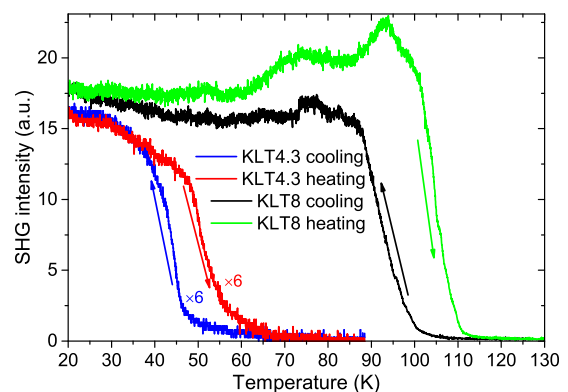


FIG. 2. Temperature dependence of the second harmonic generation (SHG) signal in KLT4.3 and KLT8 measured on zero-field cooling and heating. The SHG intensity for KLT4.3 is multiplied by a factor of 6.

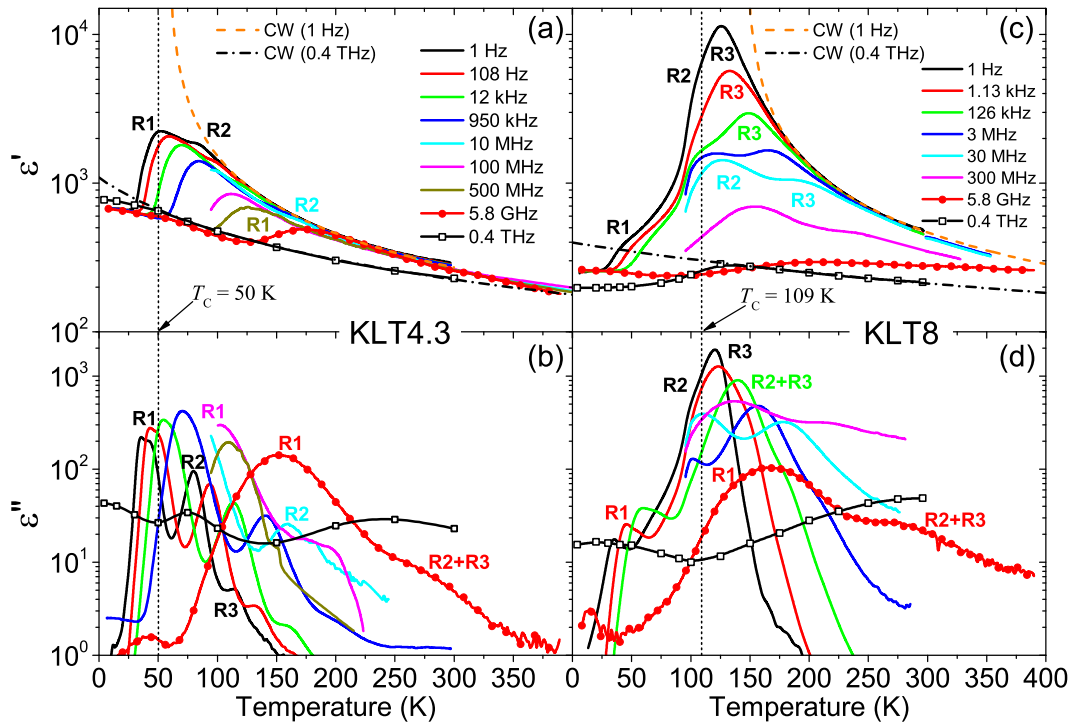


FIG. 3. Temperature dependences of (a) and (c) the dielectric permittivity and (b) and (d) dielectric loss of (a) and (b) KLT4.3 and (c) and (d) KLT8 crystals at selected frequencies from 1 Hz to 0.4 THz. Dashed and dash-dotted lines in (a) and (c) correspond to the Curie-Weiss (CW) fits of  $\varepsilon'(T)$  given by Eq. (1) at 1 Hz [CW (1 Hz)] and 0.4 THz [CW (0.4 THz)], respectively. R1, R2, and R3 mark the maxima of  $\varepsilon'(T)$  and  $\varepsilon''(T)$  corresponding to the main relaxations. The vertical dotted lines mark the phase transition temperatures according to Refs. [23,25].

generally depends on the direction of  $P_s$  with respect to the  $E$ -field polarization of the exciting laser pulse. In agreement with Ref. [17], we assume that the detected SHG power is proportional to the volume part of the FE domains with the in-plane component of  $P_s$  and to the  $P_s$  value. Its nonzero value below  $T_C$  indicates a nonzero mean  $P_s$  of the in-plane FE nanodomains within the probing laser wavelengths.

KLT4.3 shows a monotonous increase of SHG signal on cooling, like the  $P_s(T)$  dependence in Fig. 1, but for KLT8, some oscillations in the temperature dependence are seen. They are caused mainly by a phase mismatch of the first- and second-harmonic beams. The most surprising effect is the increase of SHG signal in KLT8 seen on heating. This temperature dependence was remeasured several times, and the curves shown in Fig. 2 are qualitatively reproducible. This effect should be assigned to the presence of FE domains, which are not quite frozen below  $T_C$  and change their orientation and size with time and/or temperature in the  $E$  field of the laser beam. Later in this paper, we will demonstrate that the FE phase contains some nonpolar regions with appreciable volume. The SHG results indicate that some part of the nonpolar volume might transform to polar domains on heating to  $T_C$ .

### B. Dielectric spectroscopy

Temperature-dependent dielectric permittivity and loss data at selected frequencies from 1 Hz to 0.4 THz are presented in Fig. 3. They show broad dielectric dispersions in both KLT4.3 and KLT8 which cover the whole

frequency-temperature range. The LF temperature maxima of the permittivity  $\varepsilon'(T)$  and loss  $\varepsilon''(T)$  appear near but above  $T_C$  [23,24], but the dielectric dispersion takes place both above and below  $T_C$ . The shift and splitting of the  $\varepsilon'(T)$  and  $\varepsilon''(T)$  maxima with increasing frequency show a presence of three main relaxations marked as R1, R2, and R3 in Fig. 3. At temperatures  $T \geq T_C + 60$  K, the  $\varepsilon'(T)$  at 1 Hz follows the Curie-Weiss (CW) law:

$$\varepsilon'(T) = \frac{C}{T - T_0}, \quad (1)$$

where  $T_0$  and  $C$  are the Curie temperature and Curie constant, respectively. Moreover, the dependences of  $\varepsilon'(T)$  at 0.4 THz also follow the CW law above  $T_C$  with comparable  $C$  values but much smaller  $T_0$  temperatures. Fits by the CW law of the data obtained at 1 Hz and 0.4 THz are also shown in Fig. 3 and for  $1/\varepsilon'(T)$  in Fig. 4 with the fitting parameters listed in Table I.

The permittivity at 1 Hz, if following the CW law, corresponds to the static permittivity, i.e., to the sum of all dielectric contributions of relaxations, polar phonons, and optic permittivity, which describes the usual behavior above the proper FE transition [39–41]. The CW fit at 0.4 THz corresponds to only partial Cochran-type softening of the SM [9]. When approaching  $T_C$  on cooling, deviations of the LF permittivity from the CW fit are partly due to the continuing dielectric dispersion  $< 1$  Hz (the measured  $\varepsilon'(T)$  at 1 Hz may not correspond to the static value close to  $T_C$ ), but they can be also partially assigned to the effect of PNCs with some distribution of local critical temperatures.



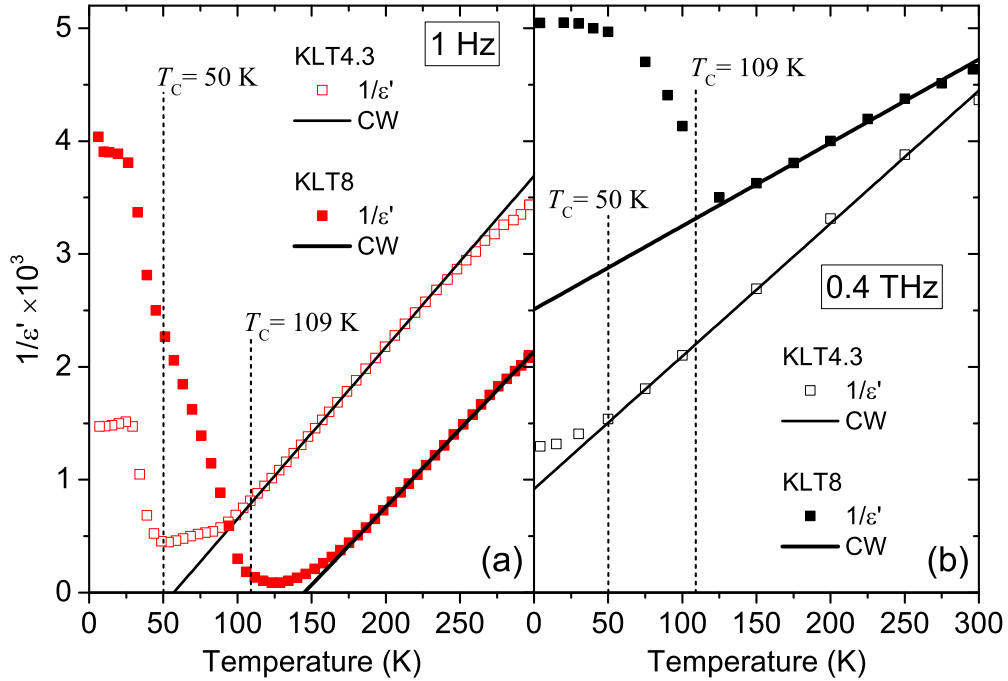


FIG. 4. Temperature dependences of the inverse dielectric permittivity of KLT4.3 (empty symbols) and KLT8 (filled symbols) at (a) 1 Hz and (b) 0.4 THz. Solid black lines correspond to the Curie-Weiss (CW) fits [Eq. (1)] of the 1 Hz and 0.4 THz  $\varepsilon'(T)$  dependences. The vertical short-dash lines mark the phase transition temperatures  $T_C = 50$  and 109 K according to Refs. [23,25].

Dielectric contributions of the relaxations to the permittivity are fully responsible for the LF maxima in  $\varepsilon'(T)$  for both KLT4.3 and KLT8. The sum of all dielectric relaxation contributions in KLT8 is much larger than that in KLT4.3. On the other hand, the dielectric contribution of phonons is larger in KLT4.3 than in KLT8, and the difference increases at lower temperatures. Below  $\sim 30$  K, all the relaxation contributions become frozen in our frequency range, and the phonon contributions dominate.

The complete set of the dielectric loss values measured in the frequency range 1 Hz–1 GHz from 10 to 350 K, selectively presented in Figs. 3(b) and 3(d), is shown in Fig. 5 in the two-dimensional frequency-temperature ( $\omega$ - $T$ ) maps, where the color represents the loss value in the logarithmic scale. The  $\omega$ - $T$  maps of the dielectric loss visualize the temperature evolution of the relaxation frequencies. The relaxations are even better seen in the AC conductivity vs  $T$  dependences  $\sigma'(T)$  at selected frequencies presented in Fig. 6, calculated from the dielectric loss spectra as

$$\sigma'(T) = 2\pi\omega\varepsilon_0\varepsilon''(T), \quad (2)$$

where  $\varepsilon_0$  is the vacuum permittivity, and  $\omega$  is the linear frequency in hertz. The AC conductivity contributions of R2 and

R3 dominate in KLT8, while that of R1 dominates in KLT4.3. The observed shifts of the local  $\sigma'(T)$  maxima are related to the temperature evolution of the mean relaxation frequencies.

For the fitting procedure of the whole measured frequency spectra, we also included the SM frequency range from the IR reflectivity and terahertz dielectric spectra of both samples. First, just the terahertz and IR spectra were simultaneously fitted in the temperature range 5–300 K using the standard factorized formula of the generalized multioscillator dielectric function [42]:

$$\varepsilon_{\text{IR}}^*(\omega) = \varepsilon'_{\text{IR}}(\omega) - i\varepsilon''_{\text{IR}}(\omega) = \varepsilon_{\infty} \prod_j \frac{\omega_{\text{LO}j}^2 - \omega^2 + i\omega\gamma_{\text{LO}j}}{\omega_{\text{TO}j}^2 - \omega^2 + i\omega\gamma_{\text{TO}j}}, \quad (3)$$

related to the normal reflectivity spectrum by the Fresnel formula:

$$R(\omega) = \left| \frac{\sqrt{\varepsilon_{\text{IR}}^*(\omega)} - 1}{\sqrt{\varepsilon_{\text{IR}}^*(\omega)} + 1} \right|^2, \quad (4)$$

where  $\varepsilon_{\infty}$  is the optical (electronic) contribution to the permittivity,  $\omega$  is the linear frequency (wave number),  $\omega_{\text{TO}j}$  and  $\omega_{\text{LO}j}$  are the frequencies of the  $j$ th transverse (TO) and longitudinal (LO) optic phonon modes, and  $\gamma_{\text{TO}j}$  and  $\gamma_{\text{LO}j}$  are their damping parameters. The resulting terahertz-IR (THz-IR) fits at selected temperatures are plotted in Figs. 7 and 8 at frequencies  $> 0.5$  THz. For fitting the lower frequency LF-HF-MW range, we must use some model for the relaxational dispersion and add it to our THz-IR response  $\varepsilon_{\text{IR}}^*(\omega)$  [Eq. (3)]. For this, we chose a sum of the Cole-Cole relaxation terms [43]:

$$\varepsilon^*(\omega) = \varepsilon'(\omega) - i\varepsilon''(\omega) = \varepsilon_{\text{IR}}^*(\omega) + \sum_j \frac{\Delta\varepsilon_j}{1 + \left(\frac{i\omega}{\omega_{\text{R}j}}\right)^{1-\alpha_j}}, \quad (5)$$

TABLE I. Parameters of the CW fits.

	$T_C$ (K)	1 Hz		0.4 THz	
		$C$ ( $10^4 \text{ K}^{-1}$ )	$T_0$ (K)	$C$ ( $10^4 \text{ K}^{-1}$ )	$T_0$ (K)
KLT4.3	50	6.58	57	8.5	-78
KLT8	109	7.25	145	13.55	-340

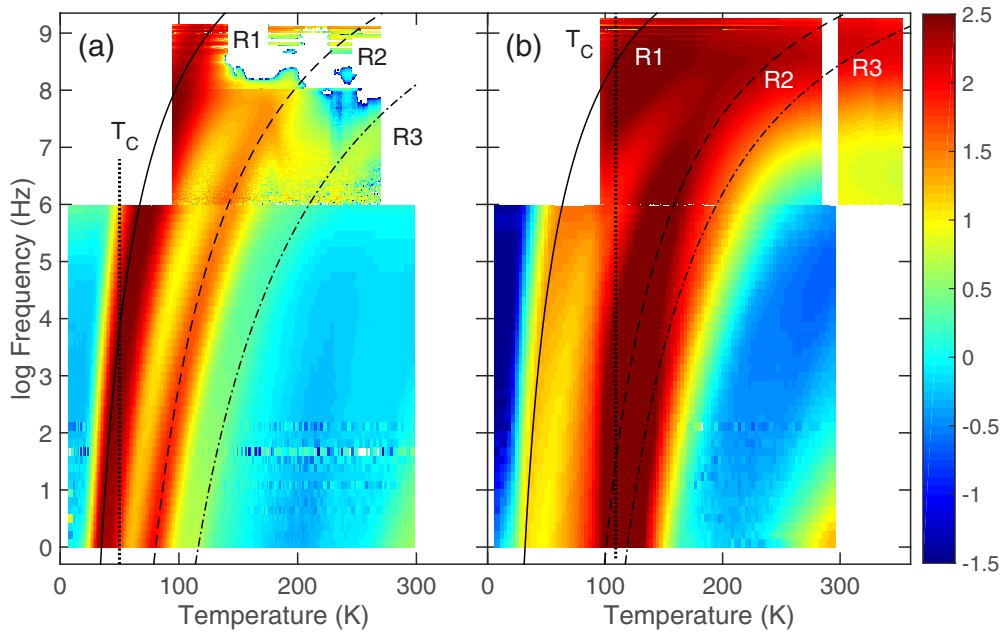


FIG. 5. Two-dimensional frequency-temperature maps of the dielectric loss of (a) KLT4.3 and (b) KLT8 crystals in the frequency range 1 Hz–1 GHz from 10 to 350 K. The color (darkness) represents the  $\log[\varepsilon''(T)]$  values. Lines are results of the Arrhenius (R1) and Vogel-Fulcher (R2, R3) fits, see Table II.

where  $\Delta\varepsilon_j$ ,  $\omega_{R_j}$ , and  $0 \leq \alpha_j \leq 1$  are the dielectric strength, mean linear relaxation frequency [maximum of the dielectric-loss function  $\varepsilon''(\omega)$ ], and the degree of broadening of the  $j$ th Cole-Cole relaxation (corresponding to a distribution of Debye relaxations [43]), respectively. Here,  $\alpha_j = 0$  corresponds to the Debye relaxation, and  $\alpha_j \rightarrow 1$  describes the infinitely broad uniform distribution of Debye relaxations

corresponding to the frequency-independent loss spectra. In our broadband dielectric spectra fits, we account for the contributions of three Cole-Cole relaxations.

The resulting spectra including the fits up to  $\sim 0.5$  THz are added to Figs. 7 and 8 and provide a smooth joining of both fitting models [Eqs. (3) and (5)]. Let us stress that it is not possible to fit the whole spectra including the THz-IR

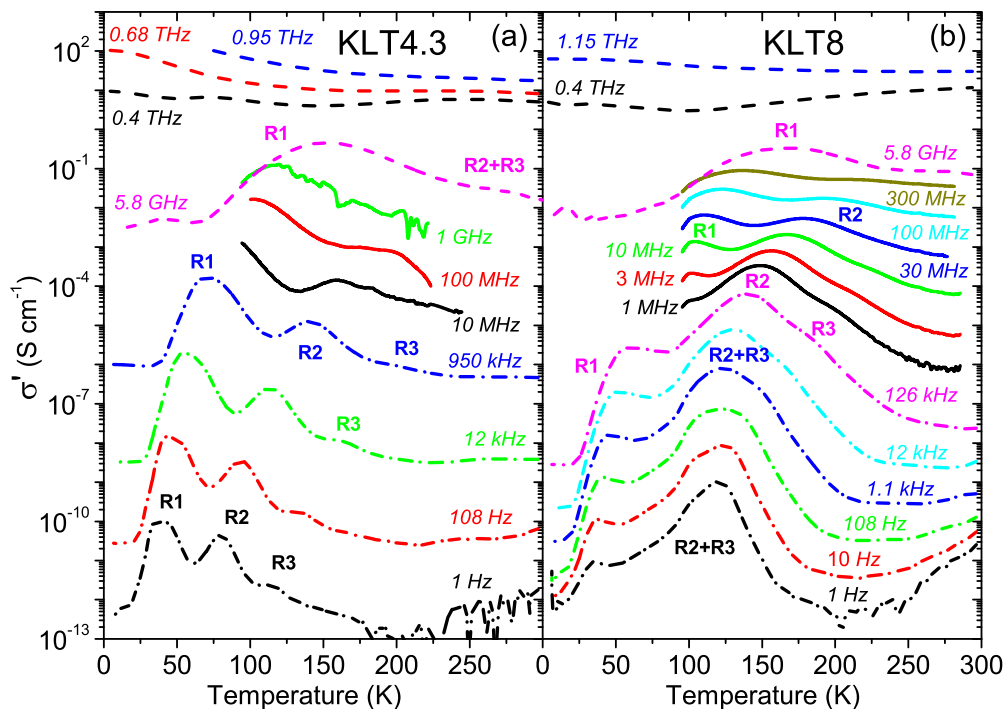


FIG. 6. Temperature dependences of the AC conductivity [calculated from Eq. (2)] of (a) KLT4.3 and (b) KLT8 crystals at selected frequencies from 1 Hz to  $\sim 1$  THz. R1, R2, and R3 mark the  $\sigma'(T)$  maxima indicating the corresponding relaxations.

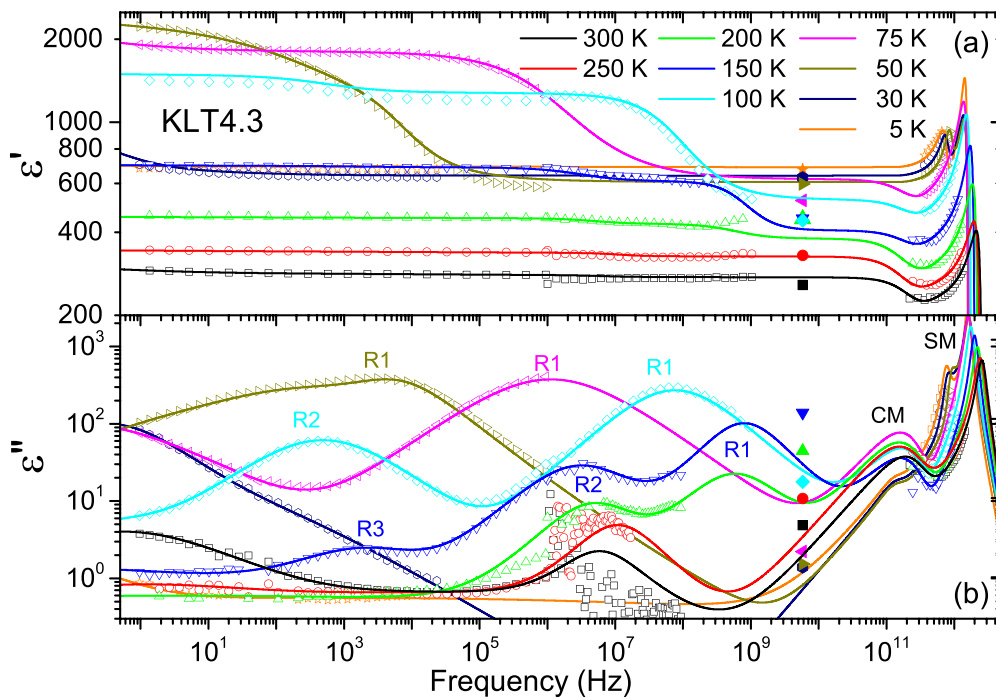


FIG. 7. Broadband dielectric spectra of (a) dielectric permittivity and (b) loss of the KLT4.3 crystal at selected temperatures. Symbols denote the experimental data, and lines correspond to the overall fits to Eqs. (3)–(5). R1, R2, R3, central mode (CM), and soft mode (SM) indicate the  $\epsilon''(\omega)$  maxima of the corresponding modes.

range to Eq. (5) because the Cole-Cole relaxations (for any  $\alpha$ ) do not obey the oscillator-strength sum rule [44,45], i.e., they contribute to the losses and AC conductivity not only around the  $\omega_{R_j}$  frequencies but unphysically strongly also for

$\omega \gg \omega_{R_j}$  up to infinite frequencies, and therefore cannot be used for fitting in the frequency range by orders of magnitude higher than  $\omega_{R_j}$ . Parameters of the central mode (CM), where no experimental data are available, were estimated in the fits

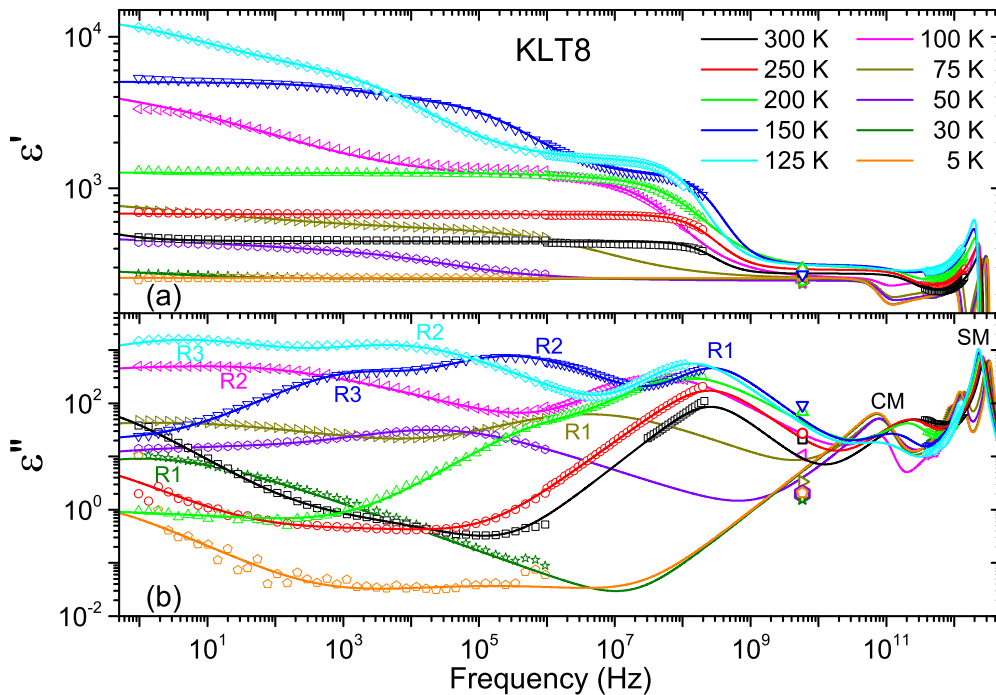


FIG. 8. Broadband dielectric spectra of (a) dielectric permittivity and (b) loss of the KLT8 crystal at selected temperatures. Symbols denote the experimental data, and lines correspond to the overall fits to Eqs. (3)–(5). R1, R2, R3, central mode (CM), and soft mode (SM) indicate the  $\epsilon''(\omega)$  maxima of the corresponding modes.

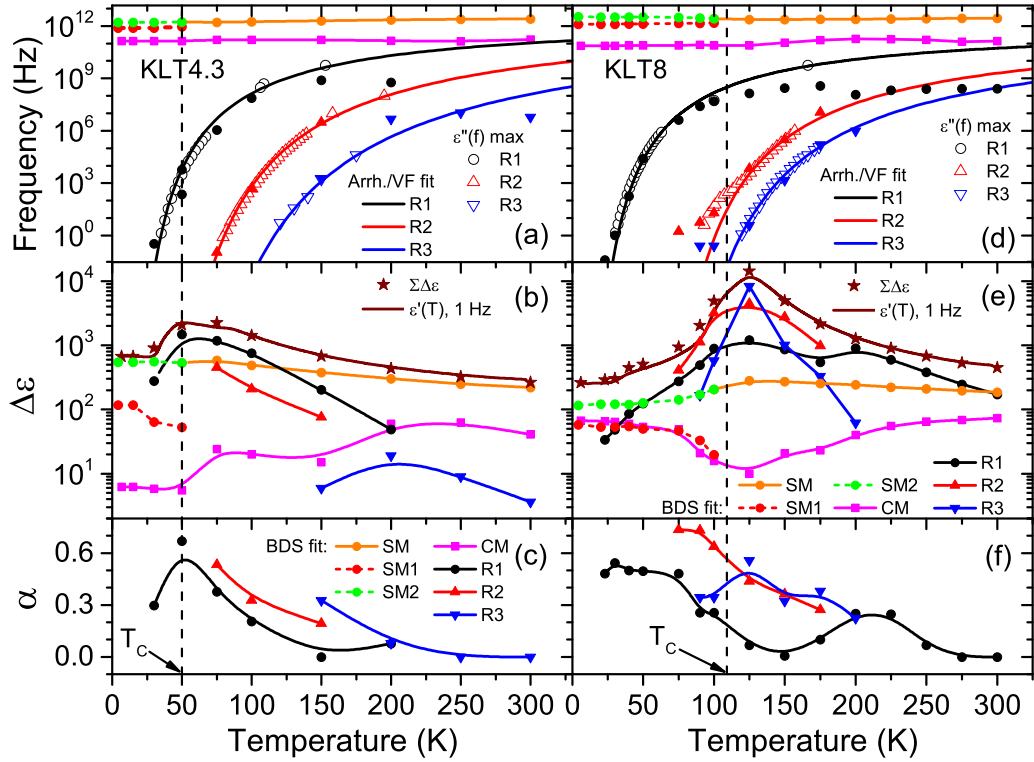


FIG. 9. Temperature dependences of the broadband dielectric spectroscopy (BDS) fit parameters of (a)–(c) KLT4.3 and (d)–(f) KLT8 crystals: (a) and (d) mean relaxation frequencies, (b) and (e) dielectric contributions, (c) and (f) Cole-Cole diffusion parameters. In (a) and (d), the frequencies corresponding to the  $\varepsilon''(\omega)$  maxima are shown (empty symbols) in addition to those from BDS fit (filled symbols); fits of the mean relaxation frequencies to the Arrhenius (for R1) and Vogel-Fulcher law (R2, R3) are shown as solid lines. In (b) and (e), the dielectric contributions of the split soft-mode (SM) components (SM1, SM2) are shown below  $T_C$ ; the sum of all contributions is compared with the experimental  $\varepsilon'(T)$  dependence at 1 Hz.

as the Debye relaxations ( $\alpha = 0$ ) accounting for the HF and terahertz permittivity data. Temperature dependences of all the fit parameters are shown in Fig. 9.

Temperature dependences of the observed three mean relaxation frequencies were fitted to Arrhenius ( $\omega_{R1}$  for R1) and Vogel-Fulcher ( $\omega_{R2,3}$  for R2, R3) laws [see Figs. 9(a) and 9(d)] with parameters listed in Table II:

$$\omega_{R1} = \omega_0 \exp\left(-\frac{E}{T}\right), \quad (6)$$

$$\omega_{R2,3} = \omega_0 \exp\left(-\frac{U}{T - T_{VF}}\right). \quad (7)$$

The imperfect fit to the 5.8 GHz dielectric loss data is forced by the fit to the gigahertz permittivity and HF-LF data. For a reasonable fit of both samples for all the temperatures, an additional excitation is needed, a CM in the  $10^{11}$  Hz range, where no measurements are available.

TABLE II. Parameters of the Arrhenius (R1) and Vogel-Fulcher (R2, R3) fits [Eqs. (6) and (7), respectively] of the mean relaxation frequencies (1 meV = 11.6 K; 1000 K = 0.086 eV).

	R1		R2		R3			
	$E$ (K)	$\omega_0$ (THz)	$U$ (K)	$T_{VF}$ (K)	$\omega_0$ (THz)	$U$ (K)	$T_{VF}$ (K)	$\omega_0$ (THz)
KLT4.3	1000	3	2000	12	5	3050	12	5
KLT8	880	1	1600	43	1	2100	43	1

### C. Raman spectroscopy

Raman spectra measured on cooling from 300 to 10 K are shown in Fig. 10 in parallel (VV) and crossed (HV) polarizations, corresponding to the  $z(xx)\bar{z}$  and  $z(yx)\bar{z}$  geometry in the Porto notation, respectively. Both crystals show qualitatively similar behavior: The Raman spectra at 300 K display features corresponding to the second-order scattering from the pure KTO crystal [46]. On cooling, new intense modes appear, signaling that a noncentrosymmetric structure develops within the crystals [47,48]. The main modes are marked in Fig. 10 with the optical mode labels of the cubic perovskite structure [46]. Interestingly, the spectra of both VV and HV polarizations at lower temperatures show a marked dissimilarity in the low-frequency range ( $<150 \text{ cm}^{-1}$ ). The difference between them is evident below  $T_C$  in both crystals. The mode with frequency  $\sim 100 \text{ cm}^{-1}$  softens from room temperature toward  $T_C$ , but below  $T_C$ , the behavior of this mode differs in the



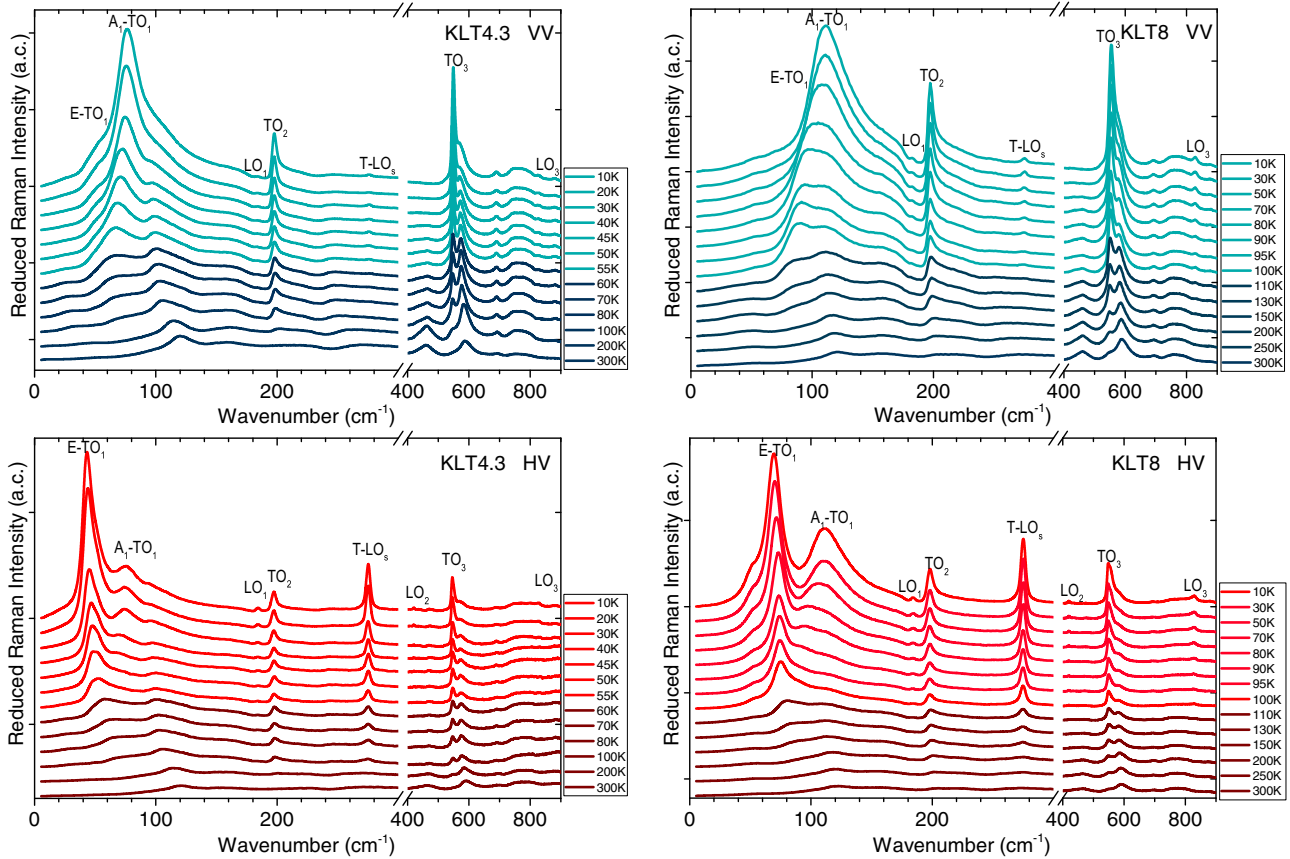


FIG. 10. Temperature-dependent Raman spectra of KLT4.3 and KLT8 in parallel (VV) and crossed (HV) polarizations.  $TO_j$  and  $LO_j$  mark  $j$ th transverse and longitudinal phonon frequencies in the low-temperature polar phase, respectively [49].  $T-LO_s$  refers to the fourth  $E$  mode and the  $B_1$  mode, both silent in the cubic phase (all modes have almost the same frequency). The splitting of the  $TO_1$  mode into the  $E$  and  $A_1$  components is also labeled.

VV and HV spectra. In the VV spectra, it starts to noticeably harden on cooling, while in the HV spectra, it splits into two components: one which further softens and a second one which hardens. This behavior of the Raman phonons speaks in favor of the development of a new structure with a predominant polar phase.

The appearance of the FE phase in the crystals is gradual, and the Raman signal from this phase is mixed with the signal from the cubic phase. On cooling, the signal from the FE phase gets stronger, although some traces of the second-order cubic Raman spectra are still present. To identify the first-order features, we subtracted the second-order Raman signal just above  $T_C$ , where it dominates, from the spectra taken in the FE phase. This procedure allowed us to follow more clearly the development of the Raman signal in the FE phase and to assign the corresponding peaks. The measured spectra contain the first-order modes corresponding to the tetragonal FE phase [47], embedded in the still existing non-FE matrix [50].

The phase transition can be well seen in the Raman experiment from the signal intensity of the spectra at selected frequencies in the HV spectra. We chose the maxima of the low-frequency peaks, corresponding to the split  $E$  and  $A_1$  components of  $TO_1$  SM. In the cubic phase, the two modes are merged into a broadband from the second-order Raman spectrum, and its intensity is almost constant, but near  $T_C$ , the

two peaks develop, and their intensity grow significantly on cooling (see Fig. 11).

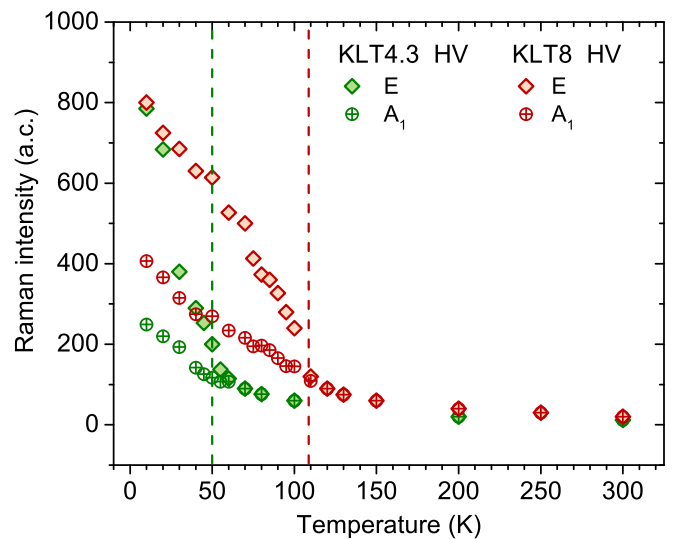


FIG. 11. Intensity of the split  $E$  and  $A_1$  modes in the Raman crossed (HV) spectra of the KLT4.3 and KLT8 crystals, stemming from the second order soft-mode Raman band in the paraelectric phase.

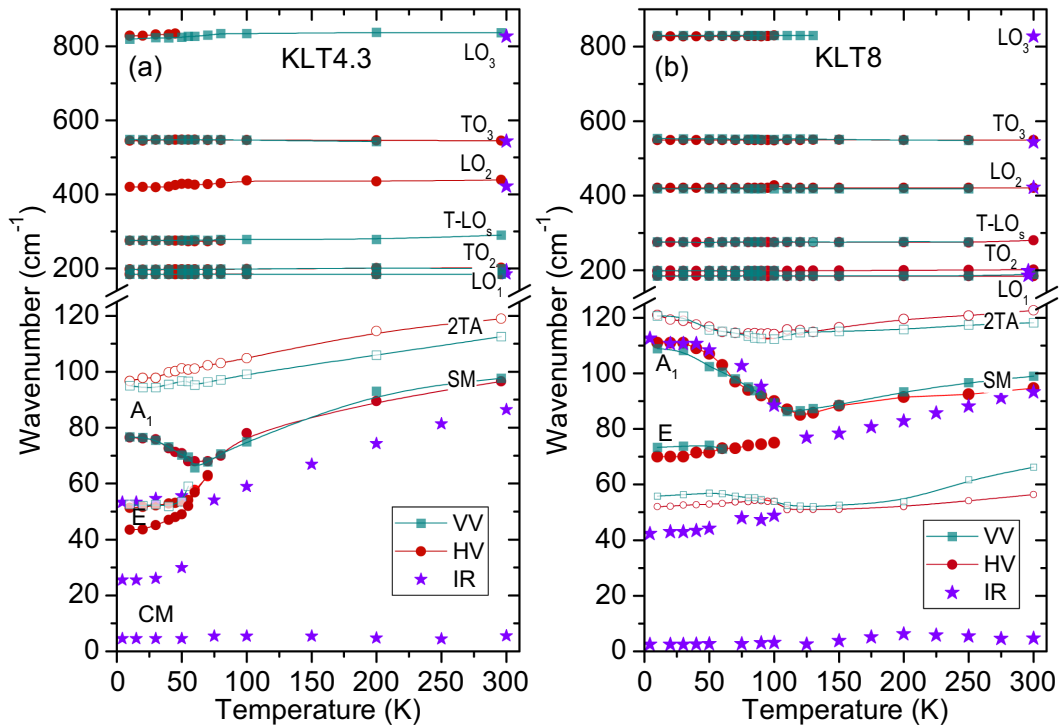


FIG. 12. Temperature dependences of the main phonon frequencies obtained from the Raman and THz-IR fits in (a) KLT4.3 and (b) KLT8. Asterisks refer to the modes determined from THz-IR fits, and squares and circles refer to Raman modes in the parallel (VV) and crossed (HV) polarization, respectively. Open symbols show second-order Raman modes. Mode labels are taken from the current literature [46,49], TA refers to the frequency of the transverse acoustic mode from the Brillouin zone boundary.

In Fig. 12, the temperature dependences of the main mode frequencies are shown together with those of the IR active modes fitted from the THz-IR spectra. Our data agree qualitatively with the Raman spectra of KLT5.4 [47] and KLT4.3 [27,28]. A careful analysis of the Raman spectra, after fitting, shows that the splitting of the low-frequency modes below  $T_C$  is also present in the VV spectra of both crystals, however with rather different intensities for VV and HV polarizations. This prompted us to investigate the angular dependence of the split Raman SM and try to reveal whether there is a preferential direction in the crystals below  $T_C$ . The results showed that this is indeed the case, see below.

Raman scattering is sensitive to the presence of clusters where the cubic symmetry is broken. As discussed in the literature [17,28,38], two types of clusters could appear due to the arrangement of Li-ion displacements: quadrupolar clusters, where the adjacent Li ions undergo antiparallel shifts and do not carry dipole moment, and probably smaller dipolar PNCs. Both types of clusters lower the symmetry to the tetragonal one and therefore can induce the splitting of Raman modes. The Raman experiment can detect the symmetry breaking already due to the presence of quadrupolar clusters on cooling at higher temperatures than other experiments (SHG) sensitive only to dipolar PNCs. One could speculate on the possibility of two transition temperatures in the temperature dependence of the Raman spectra, related to the appearance of the two types of clusters [30]. However, our Raman data reveal only one phase transition due to lowering the cubic symmetry, unlike observed in KLT5 and KLT10 ceramics [30]. The phase transition is revealed as a splitting of the SM into the  $E$  and  $A_1$

components, which is well seen in both VV and HV spectra, and the temperature dependence of their intensities in Fig. 11 does not show any change of the slope that could be assigned to appearance of other clusters. As unpolarized spectra were measured in the ceramics [30], oblique modes with mixed symmetry are detected, which might hinder a proper interpretation of the splitting.

The dissimilarity between the VV and HV Raman spectra of KLT4.3 and KLT8 at low temperatures and the SM splitting speaks in favor of the presence of a tetragonal polar phase below  $T_C$  (space group  $P4mm$ ), as generally accepted [3,8,9,26–28,47]. First-order Raman modes are symmetry forbidden in the cubic perovskites, although second-order Raman modes or modes from regions with locally broken symmetry usually appear. In the  $P4mm$  tetragonal phase of perovskites, eight first-order Raman modes ( $4E + 3A_1 + B_1$ ) are permitted by symmetry, so that they can appear below the cubic-tetragonal transition. In our case, the second-order Raman spectra at room temperature show a low-frequency SM which partially softens and splits below  $T_C$  in both samples. If the splitting of this mode corresponds to  $E + A_1$  modes of the tetragonal phase, the study of their angular dependence in the VV and HV configurations should confirm the tetragonality of the crystals. One can compare the measured angular dependences with those calculated for the  $4mm$  symmetry. To verify the symmetry of the split SM, we measured the angular dependence of the Raman scattering at 5 K. For technical reasons, it was not possible to rotate the sample inside the cryostat. Therefore, we developed a procedure in which we rotated simultaneously both the polarizer and analyzer. The result

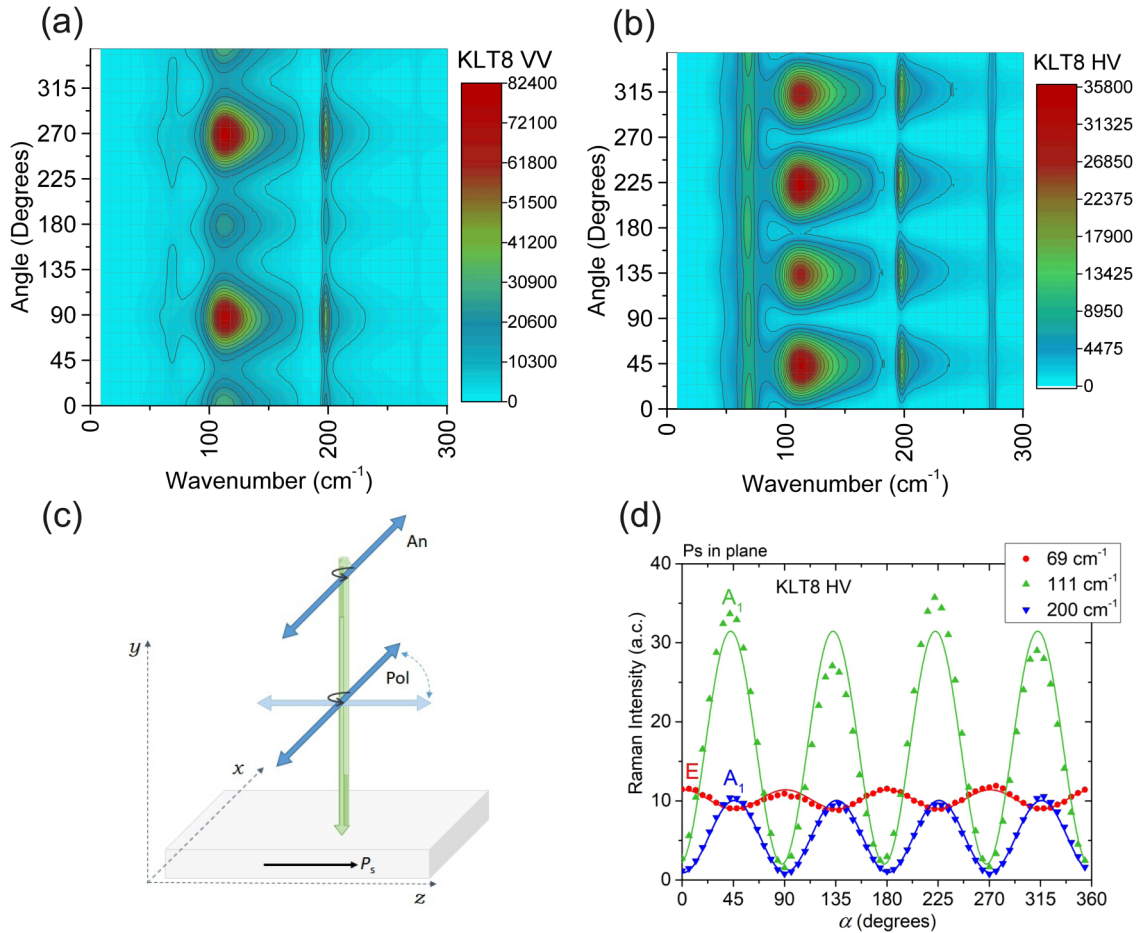


FIG. 13. Angular dependence of the Raman spectra  $<300 \text{ cm}^{-1}$  in KLT8 for parallel (VV) and crossed (HV) polarizations at 5 K. (a) and (b) The projections of the Raman intensities. (c) The geometry of the experiment is schematically presented. (d) The angular dependence of the three selected peaks in HV polarization with frequencies at 69, 111, and  $200 \text{ cm}^{-1}$  together with the corresponding fits using Eqs. (8) and (9).

is very similar to the actual rotation of the sample, albeit some small artifacts in the signal appeared. Despite this, it is possible to analyze well the main features.

The angular dependence of the Raman signal at frequencies  $<300 \text{ cm}^{-1}$  in KLT8 for VV and HV configurations at 5 K is shown in Fig. 13. The plots for VV and HV show a marked difference including different periodicity, which confirms that, at low temperature, the crystal is not cubic. The HV spectra, where the SM splitting is more evident and easier to quantify, were used for fitting the angular dependence of selected phonon frequencies. In the case of a FE crystal with  $P_s$  in the sample plane and backscattering geometry [see Fig. 13(c)], the Raman selection rules allow us to detect the  $A_1(\text{TO})$ ,  $B_1$ , and  $E(\text{TO})$  modes [51]. The intensities of these modes are modulated with respect to the rotation angle of the sample (or the polarization of the incoming beam and the scattered light from the crystal). In KTO, the  $B_1$  (silent) mode is of higher frequency ( $\sim 280 \text{ cm}^{-1}$  [52]); therefore, it is not considered in our analysis of the low-frequency split modes.

The intensity of the Raman signal is proportional to the corresponding element of the Raman tensor squared according to  $I_R \propto |\mathbf{e}_i \mathfrak{S} \mathbf{e}_s|^2$ , where  $\mathbf{e}_i$  and  $\mathbf{e}_s$  are unit vectors of the incident

and scattered beams, respectively. Here,  $\mathfrak{S}$  is the Raman tensor which depends on the crystal point group. We choose a system of axes such that the  $yz$  plane forms the input/output faces of the sample and the  $x$  axis is normal to the sample plate. In this case, the direction vectors of the incoming and outgoing beams are  $\mathbf{e}_i = (100)$ ,  $\mathbf{e}_s = (-100)$ , respectively. First, we study the case of in-plane  $P_s$ , and following the usual convention, we consider  $P_s \parallel z$ . For the tetragonal point group  $4mm$ , the corresponding Raman tensors belonging to the  $A_1$  and  $E$  symmetry modes are [51]

$$A_1(z) = \begin{pmatrix} a & 0 & 0 \\ 0 & a & 0 \\ 0 & 0 & b \end{pmatrix}, \quad E(y) = \begin{pmatrix} 0 & 0 & 0 \\ 0 & 0 & e \\ 0 & e & 0 \end{pmatrix}.$$

For evaluation of the angular dependence, we took the corresponding Raman tensor element according to the selected geometry and applied the rotation matrices  $\mathfrak{R}$  around  $x$  by the angle  $\alpha$ :

$$\mathfrak{R}(\alpha) = \begin{pmatrix} 1 & 0 & 0 \\ 0 & \cos \alpha & \sin \alpha \\ 0 & -\sin \alpha & \cos \alpha \end{pmatrix}.$$

The appropriate rotated Raman tensors for the  $A_1$  and  $E$  symmetry modes are

$$A_1(z, \alpha) = \mathfrak{R}(\alpha)A_1\mathfrak{R}^{-1}(\alpha) = \begin{pmatrix} a & 0 & 0 \\ 0 & a\cos^2\alpha + b\sin^2\alpha & (a-b)(\cos\alpha\sin\alpha) \\ 0 & (a-b)(\cos\alpha\sin\alpha) & b\cos^2\alpha \end{pmatrix},$$

$$E(y, \alpha) = \mathfrak{R}(\alpha)E\mathfrak{R}^{-1}(\alpha) = \begin{pmatrix} 0 & 0 & 0 \\ 0 & 2e\cos\alpha\sin\alpha & e(\cos^2\alpha - \sin^2\alpha) \\ 0 & e(\cos^2\alpha - \sin^2\alpha) & 2e\cos\alpha\sin\alpha \end{pmatrix}.$$

In the HV polarization,  $x(yz)x$  geometry, where the splitting is seen, we detect the Raman intensity due to the  $yz$  elements of the matrices.

In Fig. 13, we show the angular behavior at 5 K of the intensity of the split peaks at 69 and 111  $\text{cm}^{-1}$ . To check whether they obey the symmetry behavior of the  $4mm$  group, we fitted the angular dependences of their maxima with the functions calculated in the rotated tensors. The mode of  $E$  symmetry in the HV polarization should obey the following angular dependence:

$$I_E^\perp = |e(\cos^2\alpha - \sin^2\alpha)|^2, \quad (8)$$

and the mode of  $A_1$  symmetry should obey a different dependence:

$$I_{A_1}^\perp = |(a-b)(\cos\alpha\sin\alpha)|^2. \quad (9)$$

The strong  $\text{TO}_2$  mode at 200  $\text{cm}^{-1}$ , known from the IR experiment, should set the standard for the fitting of the other modes, defining its  $A_1$  or  $E$  symmetry. As seen in Fig. 13(d), its behavior corresponds to the  $A_1$  symmetry. Because the same behavior is displayed by the higher-frequency split mode at 111  $\text{cm}^{-1}$ , we conclude that this mode is the higher-frequency  $A_1$  component of the split SM. The second split mode at 69  $\text{cm}^{-1}$  corresponds to the  $E$  symmetry, as corroborated also by the fit in Fig. 13(d). Finally, let us discuss the case of out-of-plane spontaneous polarization, i.e.,  $P_s \parallel y$ . In this case, the only theoretically observable modes in the HV spectra would have the  $B_2$  symmetry, which is, however, inactive in the  $4mm$  group. In the VV spectra,  $A_1(\text{LO}) + B_1$  modes could be observed but with no angular modulation of the intensity. Since we see a strong modulation in the VV spectra with no significant constant background [Fig. 13(a)], we may infer that, in our KLT8 sample, a strongly prevailing part of domains have  $P_s$  in the sample plane.

We therefore conclude that the measured modulated Raman signal comes solely from the  $P_s$  component in the sample plane. It is known that the intensity of the  $A_1(\text{TO})$  mode in VV polarization for a sample with  $P_s$  within the sample plane is proportional to the amount of the domains with  $P_s$  along the  $z$  axis [53]. From our measurements, we can say that the KLT8 sample seems to have—within the measured volume ( $\sim 10 \mu\text{m}^3$ )—a higher amount of the microdomains at  $90^\circ$  and  $270^\circ$  from the starting rotation point [maxima of the  $A_1$ -mode intensity in Fig. 13(a)]; therefore, the domains are not randomly oriented but show a preferential direction, and the in-plane  $P_s$  is mainly perpendicular to the direction taken as the starting point of our angular measurements.

## IV. DISCUSSION

### A. Dielectric relaxations

Let us first discuss the relaxations. The fact that the Curie constant  $C$  in the CW law for 1 Hz yields approximately the same magnitude as that for the CW fit to 0.4 THz ( $\sim 10^5 \text{ K}^{-1}$ , see Table I) clearly indicates that the whole response of all the relaxations originates from their linear coupling to the SM response without appreciable additional electric charge [39], in agreement with the first-principles calculations [7,14]. This is understandable due to the small doping concentration  $x$ , which cannot change appreciably the total charge involved in the low-frequency dynamics. Our observed relaxation frequencies and their temperature dependences are in general agreement with the previously published results on KLT crystals with comparable  $x$  [3,4,10–13,23–25,38,54], summarized by Tkach *et al.* [29] for discussing their dielectric measurements on KLT5 and KLT10 ceramics, in good agreement with the data on similarly doped crystals. They analyzed their relaxation frequencies only from the temperature dependences of loss maxima at various frequencies up to 100 MHz (without fitting the spectra) and reported two relaxations (A and B), each further split in two components with slightly different temperature dependences. The high-frequency relaxation doublet ( $A_1$  and  $A_2$ ) corresponds to our R1 relaxation, but we do not see their clear splitting [see partly only in Fig. 7(b) at 50 K; at lower temperatures, it goes below our frequency range]. The low-frequency doublet (B1 and B2) corresponds roughly to our R2 and R3 relaxations, respectively.

According to our broadband fits, the highest-frequency R1 in both KLT4.3 and KLT8 from low temperatures approaches the gigahertz range near 150 K, and at higher temperatures, it remains in the same frequency range ( $10^8$ – $10^9$  Hz) and only slightly weakens but stays with nonzero dielectric strength up to 300 K [see Figs. 9(b) and 9(e)]. This differs from classical relaxors, where the relaxations emerge from the SM response only below the Burns temperature  $T_B$ , where the PNRs appear [21]. In KLT, the  $T_B$  was suggested at about  $T_C + 50$  K based on high-precision XRD [38]. Approximately below  $T_B$ , our relaxations appear to be thermally activated; however, they clearly exist even above  $T_B$  in the gigahertz range, presumably coupled to the CM. Therefore, the Burns temperature in KLT is not clearly defined. The dynamic behavior of PNCs above  $T_B$  is presently not clear in detail and needs further studies. Their existence is, however, expected since the off-centered Li ions exist up to very high temperatures. Their nonzero dielectric strength above  $T_B$  explains the tremendous difference between the  $T_0$  temperatures in the CW laws [Eq. (1)] at hertz and terahertz frequencies (see Fig. 4 and Table I), not observed in standard Pb-containing relaxors [55].



Approximately below  $T_B$ , the R1 relaxation slows down and follows the Arrhenius law with activation energy of 900–1000 K (78–86 meV) without any anomaly at  $T_C$ . Its dielectric strength undergoes a maximum near but above  $T_C$ , strongly decreasing below  $T_C$  with appreciable broadening on approaching  $T_C$  and below it. Since R1 is assigned to the  $\text{Li}^+$ -ion hopping by  $\pi/2$  (connected with several adjacent unit cells which form the PNCs and, at lower temperatures, the slightly larger PNRs) [14], it means that some of the PNRs should exist even below  $T_C$  coexisting with the FE phase, where the relaxations are frozen in the ordered FE phase. The relaxation broadening (increasing distribution of relaxation times) on cooling is due to an inhomogeneous increase in the PNR size, their mutual coupling, and the random fields caused by the frozen structural disorder [14]. The same is valid also for the R2 relaxation in the case of KLT8 (in the case of KLT4.3, it slows down below our frequency range already above  $T_C$ ), which is assigned to PNCs with Li-ion nearest-neighbor pairs hopping by  $\pi$  [14], which should be also frozen within the ordered FE phase. Let us stress that, unlike in KLT4.3, in KLT8, the R2 relaxation is stronger than R1, which might be understood by the much higher dipole moment of the latter PNCs than those around the single Li ions [14] and by the expected increasing number of PNCs with the nearest-neighbor Li-ion pairs for the higher Li concentrations [14,36].

From the behavior of the relaxations passing across  $T_C$  without any anomaly in the frequency, we may conclude that the FE phase below  $T_C$  coexists with some remains of the relaxor phase. This can be well understood by considering the percolative nature of the FE transition due to slightly increasing sizes and mutual coupling of the PNCs on cooling [18]. In this case, only such a part of the sample volume undergoes the transition, in which the PNRs percolate. Even if the coexistence of the FE and relaxor phase in KLT below  $T_C$  has been already suggested [7,23,50], nobody has tried to estimate the percolated FE volume part and its temperature dependence below  $T_C$ . The percolation threshold volume may vary from several percent up to  $>50\%$ , e.g., the well-known symmetrical Bruggeman model with spherical particles yields 33%, and the statistical three-dimensional theory yields  $\sim 16\%$  [45,56]. However, due to the metastability and nonergodicity of the FE phase in KLT [11,57–59], this value is, very probably, dependent on the specific sample, its thermal treatment, and temperature variation rate. Let us note that, also in some other doped incipient FE systems, the coexistence of the FE and relaxor phase was suggested and estimated from the temperature dependences of the nuclear magnetic resonance signal [60] or refractive indices, recalculated into contribution to  $P_s$  and its fluctuating part due to PNCs [61].

In the FE part, the PNC dipole moments undergo ordering below  $T_C$ , and the corresponding PNRs above  $T_C$  are expected to show a dynamic dipole-moment relaxation in the form of a dielectric relaxation which experiences a critical slowing down (softening) toward  $T_C$ , as expected for standard order-disorder transitions in macroscopically homogeneous materials (see, e.g., the reviews [39–41]). Such a critical slowing down at  $T_C$  combined with Arrhenius softening below  $T_C$  was observed also in the relaxor FE  $\text{PbMg}_{1/3}\text{Nb}_{2/3}\text{O}_3$ -35% $\text{PbTiO}_3$  with  $T_C = 450$  K [62]. The

percolation threshold in two-component composites with differing dielectric properties (even if independent of temperature) is also connected with a divergence of the effective static permittivity caused by the critical slowing down of a relaxation [45,56]. The R1 and R2 relaxations, since they do not reveal any critical behavior near  $T_C$ , must belong to the sample volume which does not take part in the percolation process. The relaxation R3 in KLT4.3 slows down  $<1$  Hz already  $\sim 60$  K above  $T_C$  so that we cannot discuss its behavior near  $T_C$ . In KLT8, the R3 relaxation softens below our frequency range near  $T_C$  and broadens substantially (Fig. 9) so that its behavior near and below  $T_C$  is also not clear, although its dielectric strength dominates near  $T_C$ . In principle, it could represent the expected critical relaxation with unusually slow dynamics [45,56]. The unusually slow dynamics of R3 can be understood by the specific nature of PNRs in KLT compared with those in standard relaxors since, in KLT, the centers of PNCs are fixed by the structurally frozen unit cell sites with the Li ions. It can be also related to a very slow weak variation of the permittivity (of the order of hours) after fast cooling the sample below  $T_C$ , ascribed to a very slow kinetics of the FE domain and/or PNR walls. Below  $T_C$ , this slow kinetics coexists with another process of much faster dynamics [58,59], which we assign to hopping of Li ions in PNCs (flipping of PNCs), in the relaxor volume part coexisting with the FE microdomains. In standard Pb-containing perovskite relaxors, the positions of PNRs due to the correlated off-center Pb hopping on the perovskite A sites are free, movable, and independent of chemical clusters caused by the structurally frozen B-site disorder [63]. Notwithstanding, the R3 relaxation requires further studies in the millihertz and microhertz range and/or on still higher- $x$  KLT crystals.

## B. SM and its splitting

In the paraelectric phase, the temperature softening of the SM in KLT is known to be much less pronounced than in the pure KTO, and its softening decreases with increasing  $x$ , as studied by hyper-Raman spectroscopy [9], inelastic neutron scattering [50,64,65], IR reflectivity combined with terahertz and LF spectroscopy [20,66], and terahertz spectroscopy in combination with LF dielectric data [67]. This can be understood by the influence of Li doping on the A sublattice in the perovskite structure, which does not take part in the SM eigenvector, mainly consisting of the B-site Ta displacements against the O octahedra [49], but stiffens them due to the decreasing lattice parameter on Li doping [38]. In the Raman spectra, the paraelectric SM is symmetry permitted only in the second-order scattering spectra in which the whole polar phonon branch is activated [28]. Therefore, the detected weak SM with somewhat higher frequencies than those observed in the IR response for  $T > T_C$  (by  $\sim 10$ – $20$   $\text{cm}^{-1}$ , see Fig. 12), which corresponds to some mean frequency of the soft phonon branch (see Eq. (2) in Ref. [28] for more quantitative estimates), is well understandable. From his hyper-Raman spectroscopy data, Vogt has shown [9] that the SM frequency squared (in the measured concentration and temperature range from  $x = 0$  to 0.087 and 10–170 K), which should be proportional to the mean-square polarization  $\langle P^2 \rangle$ , is proportional to  $x$  (see Fig. 6 in Ref. [9]) if the dipolar correlation length



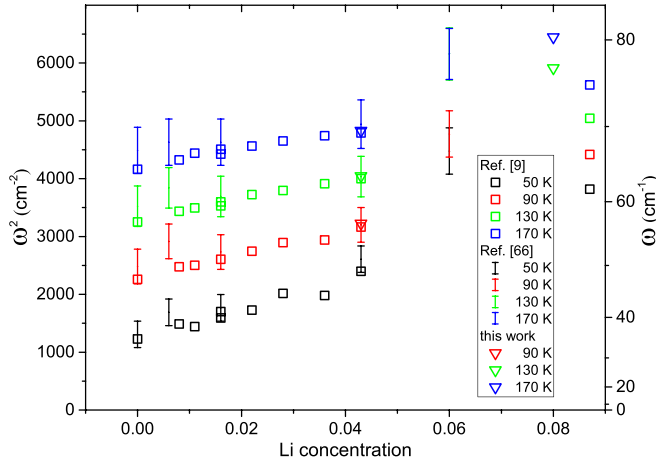


FIG. 14. Soft-mode frequencies from the THz-IR data above  $T_C$  compared with similar data on KLT6 [66] and from the hyper-Raman data [9].

is much smaller than the hyper-Raman SM wavelength. This appears to be clearly the case [26–28], but the proportionality coefficient is  $T$  dependent and decreases with increasing temperature.

In Fig. 14, we compare the SM frequencies from the IR data for  $T > T_C$  (this paper and Refs. [20,66]) with those from the hyper-Raman data [9]. Even if the accuracy of the SM frequencies from the IR reflectivity spectra is lower (see the estimated error bars in Fig. 14 corresponding to  $\omega_{SM} \pm 3 \text{ cm}^{-1}$ ), the agreement with the hyper-Raman data is satisfactory, except for the  $x = 0.06$  and  $0.08$  samples where no hyper-Raman data are available. Anyway, the hyper-Raman data of the  $x = 0.088$  sample yield somewhat lower frequency and fit better the dependence  $\omega_{SM}^2 \propto x$  suggested in Ref. [9].

In the tetragonal FE phase, one expects that the SM splits into the  $A_1$  and  $E$  components even without external bias field if the FE domains are larger than the phonon wavelength [28]. The splitting was well observed in previous Raman [9,27,28,30,47] as well as in our Raman spectra since, in the FE phase, the polar phonons are activated in the first-order scattering. However, some less pronounced and more smeared splitting could be expected even if the FE domains or PNCs/PNRs are much smaller than the probing light wavelength, as follows from modeling using the effective medium approximation (EMA), which can be applied in such cases [55]. The fact that no SM splitting was observed (in zero bias field) in the hyper-Raman spectra [28] nor in the IR reflectivity [20,66] shows that the PNCs and FE domains are much smaller than the probing wavelengths. It supports also the idea that not the whole sample volume undergoes the FE transition [7,18,23,50] since the corresponding spectra are also sensitive to the non-FE part of the sample, unlike in Raman spectra, where this sample part is inactive in the first-order scattering.

Our fits below  $T_C$  have revealed two SM components and, additionally, a CM in the 100 GHz range, required by the fit. The lower-frequency and weaker SM component does not correspond to any of the  $A_1$  and  $E$  components seen in the Raman spectra. We assign it to the SM corresponding to the non-FE part of our samples, not active in the Raman spectra.

As expected for this assignment, it continues softening below  $T_C$  (from  $\sim 31$  to  $\sim 26 \text{ cm}^{-1}$  for KLT4.3 and from  $\sim 48$  to  $\sim 41 \text{ cm}^{-1}$  for KLT8, see Fig. 12), but the frequencies still remain higher than those in pure KTO [52]. The high-frequency SM component from our fits is close to the  $E$  component of the split Raman SM in the KLT4.3 sample but close to the  $A_1$  Raman SM component in the KLT8 sample (Fig. 12). Like in the hyper-Raman spectra without bias field, no clear  $A_1$ - $E$  SM splitting is seen in either of the THz-IR spectra. Unlike in the THz-IR spectra, the hyper-Raman SM frequencies are close to those of the  $E$  components of the Raman SM for all  $x$  [9]. A possible explanation for this difference can result from our Raman spectra analysis, which indicates that, in our KLT8 sample,  $P_s$  lies mostly within the sample plane. As the  $E$  field of our transverse terahertz and IR wave probe lies only in this plane, it can detect predominantly the  $A_1$  component of the spectra.

Since according to many experiments [4,7,10,11,17,28,36,57,59] even below  $T_C$  without external  $E$  field the sizes of single-domain FE and PNC regions are substantially smaller than the optical wavelengths, we may apply EMA modeling for simulating and fitting the split SM below  $T_C$  in our THz-IR spectra. As in the case of classical relaxors, where our approach was already successfully used for analyzing the anisotropic local THz-IR dielectric response of PNRs in  $\text{Pb}(\text{Mg}_{1/3}\text{Nb}_{2/3})\text{O}_3$  [68,69] and  $\text{Pb}(\text{Mg}_{1/3}\text{Ta}_{2/3})\text{O}_3$  [55], we use the Bruggeman approach [45,70,71], which assumes that the sufficiently small spherical particles of both components are embedded into an effective medium, which assures the spatial independent probing field within all individual particles, required by the EMA model. Such systems are equivalent within EMA to a composite of isotropic particles whose dielectric responses are equal to principle dielectric responses of the anisotropic crystallite [72]. Since in addition to the  $A_1$  and  $E$  SM components we have also the third non-FE component of the SM, our modeling proceeded in two steps. In the first step, we took the  $A_1$  and  $E$  SM frequencies and damping constants from our Raman spectra and fitted their strengths to our THz-IR spectra above  $\sim 50 \text{ cm}^{-1}$  to obtain the effective dielectric SM response of the FE volume part ( $\epsilon_{FE}$ ):

$$(1 - x_{A_1}) \frac{\epsilon_E - \epsilon_{FE}}{\epsilon_E + 2\epsilon_{FE}} + x_{A_1} \frac{\epsilon_{A_1} - \epsilon_{FE}}{\epsilon_{A_1} + 2\epsilon_{FE}} = 0. \quad (10)$$

In the second step, we added to this part the non-FE regions ( $x_{KTO}$ ) with the dielectric response  $\epsilon_{KTO}$ , taking the frequency and damping of the THz-IR SM from the data on pure KTO [73], to obtain the effective dielectric response of our modeling ( $\epsilon_{eff}$ ):

$$(1 - x_{KTO}) \frac{\epsilon_{FE} - \epsilon_{eff}}{\epsilon_{FE} + 2\epsilon_{eff}} + x_{KTO} \frac{\epsilon_{KTO} - \epsilon_{FE}}{\epsilon_{KTO} + 2\epsilon_{FE}} = 0. \quad (11)$$

Parameters of the SM components and their fitted volume parts taken for the EMA modeling are listed in Table III.

The EMA-modeled effective SM dielectric spectra for selected temperatures together with those from our standard oscillator fitting (see Figs. 7–9) are shown in Figs. 15 and 16. In Fig. 15(c), we plot our measured THz-IR reflectivity spectra of KLT4.3 at 10 K together with the fitted and modeled reflectivity spectra. The modeled effective reflectivity is much

TABLE III. Parameters of the SM components for KLT4.3 and KLT8 from our Raman spectra and of KTO ceramics from Ref. [73] used for the Bruggeman EMA modeling.

	KLT4.3		KLT8		
	10 K	50 K	10 K	50 K	90 K
$\omega_E$ (cm <sup>-1</sup> )	45	48	73	74	74
$\gamma_E$ (cm <sup>-1</sup> )	8	8	17	12	13
$\omega_{A_1}$ (cm <sup>-1</sup> )	76.5	71	108	102	93
$\gamma_{A_1}$ (cm <sup>-1</sup> )	25	27	23	24	37
$\omega_{SM-KTO}$ (cm <sup>-1</sup> )	23	32	23	32	47
$\gamma_{SM-KTO}$ (cm <sup>-1</sup> )	4.5	5.5	4.5	5.5	7.5
$x_{A_1}$	0.6	0.6	0.9	0.9	0.9
$x_{KTO}$	0.17	0.17	0.057	0.057	0.057

closer to the measured one compared with the fitted reflectivity, and in agreement with the experiment, it does not show the pronounced reflectivity minimum  $\sim 50$  cm<sup>-1</sup>, unlike the

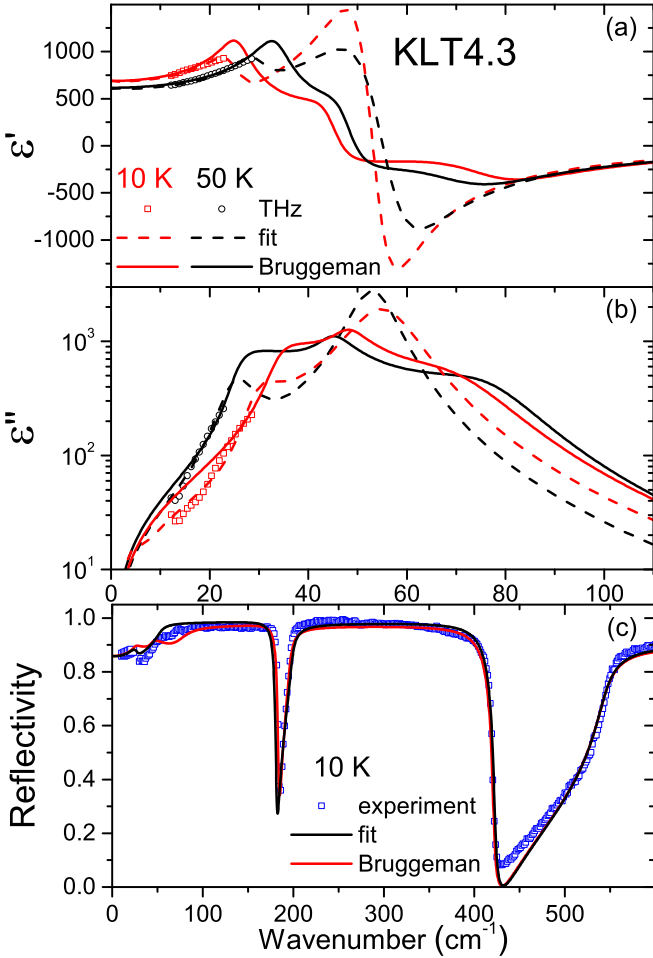


FIG. 15. (a) and (b) Complex dielectric spectra for KLT4.3 from standard oscillator fitting using Eqs. (3) and (4) (dashed lines, see Figs. 7–9) along with the results of Bruggeman modeling [Eqs. (10) and (11), solid lines] and terahertz (THz) experimental data (symbols) for 10 and 50 K. (c) Terahertz and IR experimental data (symbols), fitted and modeled reflectivity spectra (lines) for 10 K.

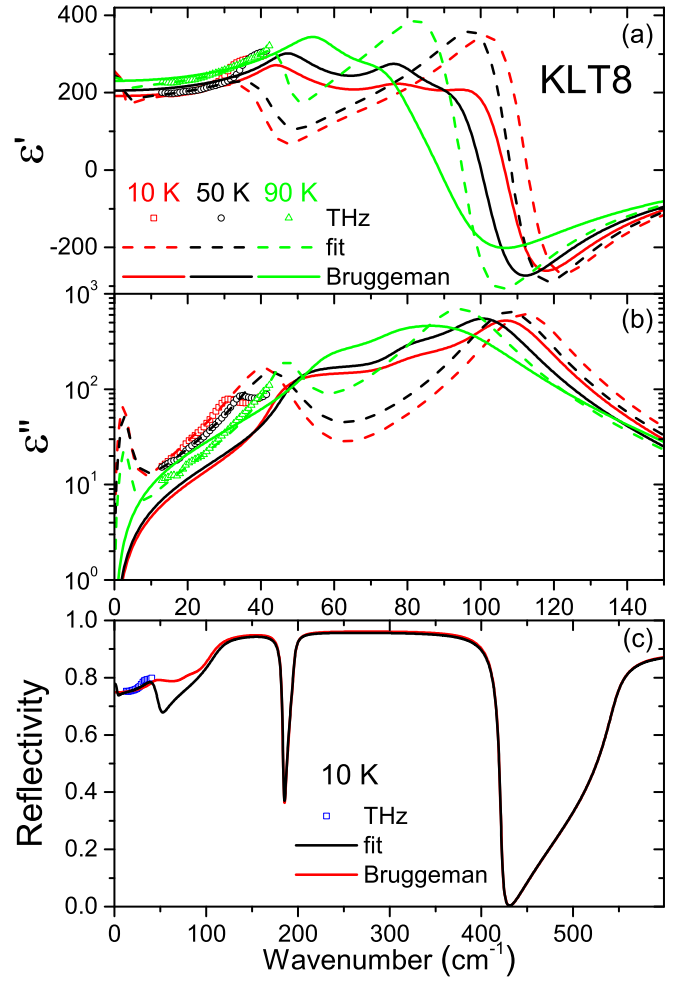


FIG. 16. (a) and (b) Complex dielectric spectra for KLT8 from standard oscillator fitting using Eqs. (3) and (4) (dashed lines, see Figs. 7–9) along with the results of Bruggeman modeling [Eqs. (10) and (11), solid lines] and terahertz (THz) experimental data (symbols) for 10, 50, and 90 K. (c) Terahertz experimental data (symbols), fitted and modeled reflectivity spectra (lines) for 10 K.

standardly fitted THz-IR spectra. Let us note that we do not show the corresponding experimental IR reflectivity of the KLT8 at 10 K since our sample was too small for reliable measurements in the low-frequency IR range. In the high-frequency IR range, the spectra of KLT8 reproduce the same features as the KLT4.3 and undoped KTO [20,73], which shows that the higher-frequency hard TO and LO modes in KLT are almost independent of  $x$  and  $T$ .

We should emphasize that, for our modeling, we did not fix the volume fraction  $x_{A_1} = \frac{1}{3}$  ( $x_E = \frac{2}{3}$ ), as would correspond to the random statistical distribution of tetragonal FE nanodomains, but we have used  $x_{A_1}$  as a free fitting parameter. Its higher-volume fractions indicate that the sample plane, which only is probed by our IR experiment, contains more domains with  $P_s$  in this plane than corresponds to random domain orientations. This result was fully confirmed by the angular dependence of our Raman spectra of KLT8 and might be caused by some mechanical clamping of the samples during the cooling. Concerning the non-FE volume fraction  $x_{KTO}$ , it

was possible to fit it independently of the temperature below  $T_C$ , which is presumably not a very plausible scenario for the non-FE part below the percolated FE phase transition. Since the fitting procedure is not completely unambiguous, we cannot take its value too literally. Therefore, the non-FE volume part in KLT and its temperature dependence below  $T_C$  require further studies. Nevertheless, the success of our EMA modeling of the IR response can clarify the long-time controversy between the SM splitting in Raman spectra of KLT not observed in the hyper-Raman spectra, as discussed in a more qualitative way by Vogt [28].

Let us comment on the appearance and behavior of the CM whose existence must be inferred from the difference between the terahertz permittivity at the low-frequency tail and higher permittivity above the relaxation frequencies  $\sim 1$  GHz. The CM was fitted to a Debye relaxation in the  $10^{11}$  Hz range with a dielectric strength of 10–100, slowly vanishing below  $T_C$  in the case of KLT4.3, but with appreciable strengths down to the lowest temperatures in the case of KLT8, where all the thermally activated relaxations are already frozen (Fig. 9). So far, it was observed only as a low-frequency dielectric loss increase in the terahertz spectra of the KLT6 at 300 K in [20]. The CM is not thermally activated and does not appear in the undoped KTO [73]. A similar excitation (even stronger for some compositions and temperatures) was recently observed in the BaTiO<sub>3</sub>-BaZrO<sub>3</sub> solid solution [74], but its strength tends to vanish at low temperatures. In both systems, it could be assigned to so-called quasi-Debye losses, which were theoretically predicted for anharmonic noncentrosymmetric structures as due to fluctuations of the thermal phonon density distribution function, whose frequency is given by the mean damping of the thermal phonons [75].

## V. CONCLUSIONS

We have demonstrated that the broadband dielectric spectroscopy from 1 Hz to 10 THz combined with Raman spectroscopy is essential for understanding the complex dynamics of PNRs and mechanism of the unusual percolative FE transition in KLT where the FE and relaxor regions coexist.

Particularly from the behavior of the two observed thermally activated Cole-Cole relaxations following the Arrhenius or Vogel-Fulcher law without frequency anomalies at  $T_C$ , it was confirmed that only part of the sample volume undergoes the FE transition, as expected from the percolative nature of the FE transition. These relaxations, assigned to the flipping dynamics of PNRs in the non-FE relaxor volume parts, remain active up to room temperature in the gigahertz spectral range, so that no standardly defined Burns temperature can be introduced for KLT. A third relaxation of lower frequency was tentatively assigned to the critical relaxation connected with the percolative nature of the FE transition.

The non-FE part below  $T_C$  is revealed in the terahertz spectra as a low-frequency SM component in the 30–50 cm<sup>-1</sup> range. The strongly reduced SM softening on cooling compared with the undoped KTO, known from the hyper-Raman spectroscopy, was confirmed by the THz-IR spectroscopy. The FE SM part below  $T_C$  undergoes the expected splitting into  $E$  and  $A_1$  components due to the tetragonal symmetry, clearly seen in the polarized Raman spectra and proven by their angular dependence at low temperature, but not clearly revealed in the IR reflectivity. Modeling the split THz-IR SM response below  $T_C$  (taken partly from the Raman response) using the EMA approach with Bruggeman model has explained why the splitting can hardly be seen in the IR reflectivity spectra if the FE domains and PNRs are much smaller than the wavelengths of probing light. In the same way, the long-time controversy about the absence of SM splitting in the hyper-Raman spectra is also clarified. Comparison of the gigahertz and terahertz permittivity indicates the presence of the CM in the  $10^{11}$  Hz range in the whole temperature range, assigned to the quasi-Debye losses.

## ACKNOWLEDGMENTS

This paper is supported by the Czech Science Foundation (Project No. 21-06802S), MŠMT project (SOLID21-CZ.02.1.01/0.0/0.0/16\_019/0000760), and Grant Agency of the Czech Technical University in Prague (Project No. SGS22/182/OHK4/3T/14).

- 
- [1] Y. Yacoby and S. Just, *Solid State Commun.* **15**, 715 (1974).
  - [2] W. Kleemann, S. Kütz, and D. Rytz, *Europhys. Lett.* **4**, 239 (1987).
  - [3] U. T. Höchli, K. Knorr, and A. Loidl, *Adv. Phys.* **39**, 405 (1990).
  - [4] W. Kleemann, J. Dec, S. Miga, and D. Rytz, *Z. Kristallogr.* **226**, 145 (2011).
  - [5] G. A. Samara, *J. Phys.: Condens. Matter* **15**, R367 (2003).
  - [6] S. E. Rowley, L. J. Spalek, R. P. Smith, M. P. M. Dean, M. Itoh, J. F. Scott, G. G. Lonzarich, and S. S. Saxena, *Nat. Phys.* **10**, 367 (2014).
  - [7] G. Geneste, J. M. Kiat, H. Yokota, Y. Uesu, and F. Porcher, *Phys. Rev. B* **81**, 144112 (2010).
  - [8] H. Vogt, *Ferroelectrics* **184**, 31 (1996).
  - [9] H. Vogt, *Ferroelectrics* **202**, 157 (1997).
  - [10] H. M. Christen, U. T. Hochli, A. Chatelain, and S. Ziolkiewicz, *J. Phys.: Condens. Matter* **3**, 8387 (1991).
  - [11] P. Doussineau, Y. Farssi, C. Frenois, A. Levelut, K. Mcenaney, J. Toulouse, and S. Ziolkiewicz, *Europhys. Lett.* **24**, 415 (1993).
  - [12] R. K. Pattnaik, J. Toulouse, and B. George, *Phys. Rev. B* **62**, 12820 (2000).
  - [13] S. A. Prosandeev, V. A. Trepakov, M. E. Savinov, L. Jastrabik, and S. E. Kapphan, *J. Phys.: Condens. Matter* **13**, 9749 (2001).
  - [14] S. A. Prosandeev, E. Cockayne, and B. P. Burton, *Phys. Rev. B* **68**, 014120 (2003).
  - [15] G. Yong, J. Toulouse, R. Erwin, S. M. Shapiro, and B. Hennion, *Phys. Rev. B* **62**, 14736 (2000).
  - [16] H. Yokota, T. Oyama, and Y. Uesu, *Phys. Rev. B* **72**, 144103 (2005).
  - [17] G. A. Azzini, G. P. Banfi, E. Giulotto, and U. T. Hochli, *Phys. Rev. B* **43**, 7473 (1991).
  - [18] S. A. Prosandeev, V. S. Vikhnin, and S. Kapphan, *Eur. Phys. J. B* **15**, 469 (2000).

- [19] M. Stachiotti, R. Migoni, J. Kohanoff, and U. T. Hochli, *Ferroelectrics* **157**, 335 (1994).
- [20] V. Železný, A. Pashkin, J. Petzelt, M. Savinov, V. Trepakov, and S. Kapphan, *Ferroelectrics* **302**, 195 (2004).
- [21] V. Bovtun, V. Porokhonskyy, M. Savinov, A. Pashkin, V. Železný, and J. Petzelt, *J. Eur. Ceram. Soc.* **24**, 1545 (2004).
- [22] A. Pashkin, Ph.D. Thesis, Prague (2004).
- [23] Z. Trybuła, J. Dec, S. Miga, S. Łoś, and M. Trybuła, *Mat. Res. Bull.* **84**, 298 (2016).
- [24] Z. Trybuła, S. Łoś, S. Miga, W. Kempniński, J. Dec, and M. Trybuła, *Mat. Chem. Phys.* **219**, 278 (2018).
- [25] Z. Trybuła, S. Łoś, M. Trybuła, J. Dec, and S. Miga, From relaxor to ferroelectric behavior in  $K_{1-x}Li_xTaO_3$ , 2016 *Joint IEEE International Symposium on the Applications of Ferroelectrics, European Conference on Application of Polar Dielectrics, and Piezoelectric Force Microscopy Workshop (ISAF/ECAPD/PFM)* (IEEE, Darmstadt, Germany, 2016), pp. 1–4.
- [26] H. Vogt, *Phys. Rev. B* **58**, 9916 (1998).
- [27] H. Vogt, *Ferroelectrics* **239**, 165 (2000).
- [28] H. Vogt, *J. Phys.: Condens. Matter* **13**, 4313 (2001).
- [29] A. Tkach, A. Almeida, J. A. Moreira, A. Espinha, M. R. Chaves, J. P. de la Cruz, and P. M. Vilarinho, *J. Phys. D: Appl. Phys.* **44**, 315406 (2011).
- [30] A. Tkach, A. Almeida, J. A. Moreira, M. R. Chaves, A. Espinha, and P. M. Vilarinho, *J. Phys.: Condens. Matter* **24**, 045906 (2012).
- [31] J. J. Van der Klink and D. Rytz, *J. Cryst. Growth* **56**, 673 (1982).
- [32] V. Bovtun, V. Pashkov, M. Kempa, S. Kamba, A. Eremenko, V. Molchanov, Y. Poplavko, Y. Yakymenko, J. H. Lee, and D. G. Schlom, *J. Appl. Phys.* **109**, 024106 (2011).
- [33] V. Bovtun, S. Veljko, A. Axelsson, S. Kamba, N. Alford, and J. Petzelt, *Integr. Ferroelectr.* **98**, 53 (2008).
- [34] J. Krupka, *Meas. Sci. Technol.* **17**, R55 (2006).
- [35] P. Kužel, H. Němec, F. Kadlec, and C. Kadlec, *Opt. Express* **18**, 15338 (2010).
- [36] P. Voigt, K. Betzler, N. Schmidt, and S. Kapphan, *Ferroelectrics* **106**, 149 (1990).
- [37] P. Voigt and S. Kapphan, *J. Phys. Chem. Solids* **55**, 853 (1994).
- [38] H. Yokota, Y. Uesu, C. Malibert, and J.-M. Kiat, *Phys. Rev. B* **75**, 184113 (2007).
- [39] J. Petzelt, G. V. Kozlov, and A. A. Volkov, *Ferroelectrics* **73**, 101 (1987).
- [40] E. Buixaderas, S. Kamba, and J. Petzelt, *Ferroelectrics* **308**, 131 (2004).
- [41] S. Kamba, *APL Mater.* **9**, 020704 (2021).
- [42] R. P. Lowndes, *Phys. Rev. B* **1**, 2754 (1970).
- [43] S. Kamba, V. Bovtun, J. Petzelt, I. Rychetský, R. Mizaras, A. Brilingas, J. Banys, J. Grigas, and M. Kosec, *J. Phys.: Condens. Matter* **12**, 497 (2000).
- [44] D. Y. Smith, in *Handbook of Optical Constants in Solids*, edited by E. D. Palik (Academic Press, Burlington, 1985), Vol. 1, Chap. 3, pp. 35–68.
- [45] J. Petzelt, D. Nuzhnyy, V. Bovtun, M. Savinov, M. Kempa, and I. Rychetský, *Phys. Status Solidi A* **210**, 2259 (2013).
- [46] W. G. Nilsen and J. G. Skinner, *J. Chem. Phys.* **47**, 1413 (1967).
- [47] R. L. Prater, L. L. Chase, and L. A. Boatner, *Phys. Rev. B* **23**, 5904 (1981).
- [48] H. Uwe, K. B. Lyons, H. L. Carter, and P. A. Fleury, *Phys. Rev. B* **33**, 6436 (1986).
- [49] J. Hlinka, J. Petzelt, S. Kamba, D. Noujni, and T. Ostapchuk, *Phase Transitions* **79**, 41 (2006).
- [50] S. Wakimoto, G. A. Samara, R. K. Grubbs, E. L. Venturini, and L. A. Boatner, *Nucl. Instr. Meth. Phys. Res. A* **600**, 254 (2009).
- [51] R. Loudon, *Adv. Phys.* **13**, 423 (1964).
- [52] H. Vogt and H. Uwe, *Phys. Rev. B* **29**, 1030 (1984).
- [53] T. Sakashita, H. Chazono, and G. Pezzotti, *J. Appl. Phys.* **102**, 124106 (2007).
- [54] V. Laguta, M. Glinchuk, I. Kondakova, and Z. Trybuła, *Ferroelectrics* **298**, 171 (2004).
- [55] D. Nuzhnyy, J. Petzelt, V. Bovtun, S. Kamba, and J. Hlinka, *Appl. Phys. Lett.* **114**, 182901 (2019).
- [56] C.-W. Nan, Y. Shen, and J. Ma, *Ann. Rev. Mater. Res.* **40**, 131 (2010).
- [57] P. Doussineau, A. Levelut, and S. Ziolkiewicz, *Europhys. Lett.* **33**, 391 (1996).
- [58] P. Doussineau, T. de Lacerda-Aroso, and A. Levelut, *J. Phys.: Condens. Matter* **12**, 1461 (2000).
- [59] F. Alberici-Kious, J. P. Bouchaud, L. F. Cugliandolo, P. Doussineau, and A. Levelut, *Phys. Rev. B* **62**, 14766 (2000).
- [60] S. Rod and J. J. van der Klink, *Phys. Rev. B* **49**, 15470 (1994).
- [61] P. A. Markovin, V. A. Trepakov, M. E. Guzhva, O. E. Kvyatkovskii, A. G. Razdobarin, and M. Itoh, *Ferroelectrics* **538**, 35 (2019).
- [62] V. Bovtun, S. Kamba, S. Veljko, D. Nuzhnyy, J. Kroupa, M. Savinov, P. Vaněk, J. Petzelt, J. Holc, M. Kosec, H. Amorín, and M. Alguero, *Phys. Rev. B* **79**, 104111 (2009).
- [63] J. Hlinka, *J. Adv. Diel.* **2**, 1241006 (2012).
- [64] R. S. Klein, G. E. Kugel, and B. Hennion, *J. Phys.: Condens. Matter* **8**, 1109 (1996).
- [65] S. Wakimoto, G. A. Samara, R. K. Grubbs, E. L. Venturini, L. A. Boatner, G. Xu, G. Shirane, and S. H. Lee, *Phys. Rev. B* **74**, 054101 (2006).
- [66] J. Petzelt, S. Kamba, V. Bovtun, and A. Pashkin, *Ferroelectrics* **298**, 219 (2004).
- [67] Y. Ichikawa and K. Tanaka, *Phys. Rev. B* **77**, 144102 (2008).
- [68] J. Hlinka, T. Ostapchuk, D. Noujni, S. Kamba, and J. Petzelt, *Phys. Rev. Lett.* **96**, 027601 (2006).
- [69] D. Nuzhnyy, J. Petzelt, V. Bovtun, M. Kempa, S. Kamba, J. Hlinka, and B. Hehlen, *Phys. Rev. B* **96**, 174113 (2017).
- [70] D. J. Bergman, *Phys. Rep.* **43**, 377 (1978).
- [71] J. Petzelt, I. Rychetský, and D. Nuzhnyy, *Ferroelectrics* **426**, 171 (2012).
- [72] D. Stroud, *Phys. Rev. B* **12**, 3368 (1975).
- [73] S. Glinšek, D. Nuzhnyy, J. Petzelt, B. Malič, S. Kamba, V. Bovtun, M. Kempa, V. Skoromets, P. Kužel, I. Gregora, and M. Kosec, *J. Appl. Phys.* **111**, 104101 (2012).
- [74] J. Petzelt, V. Bovtun, D. Nuzhnyy, M. Kempa, M. Savinov, M. Paściak, S. Kamba, G. Canu, and V. Buscaglia, *Phys. Status Solidi B* **258**, 2100259 (2021).
- [75] V. L. Gurevich and A. K. Tagantsev, *Adv. Phys.* **40**, 719 (1991).